Numerical study of three-dimensional incompressible thermal flows in complex geometries

Part I: theory and benchmark solutions

Received January 1995
Revised September 1996

Balasubramaniam Ramaswamy
Department of Mechanical and Environmental Engineering, University of California at Santa Barbara, California, USA, and
Rafael Moreno
Exxon Production Research Company, Houston, Texas, USA

Nomenclature

x^*, y^*, z^*	=	co-ordinate system with nodal origin
u^*	=	horizontal velocity in the x^* direction
v^*	=	vertical velocity in the y^* direction
w^*	=	velocity in the z^* direction
p^*	=	pressure
t^*	=	time
x, y, z	=	non-dimensional co-ordinate system with nodal origin
t	=	non-dimensional time
U	=	reference velocity
g	=	gravitational acceleration
Δt	=	time step
ppp	=	non-dimensional pressure at the cell centres
X, M	=	unknown quantities
a, b, c, d, e, f, s	=	coefficients
A, B, C, D, E, F	=	coefficients
U_1, U_2, U_3, U_4	=	coefficients
V_1, V_2, V_3, V_4	=	coefficients
W_1, W_2, W_3, W_4	=	coefficients
c_1 to c_{20}	=	coefficients

Greek letters

α	=	thermal diffusivity
β	=	thermal expansion coefficient
ρ	=	density
μ	=	viscosity
ν	=	kinematic viscosity
ε	=	iterative error
ω	=	over-relaxation parameter
$\omega_{\bar{u}}$	=	over-relaxation parameter for $\bar{u}$ calculation
$\omega_{\bar{v}}$	=	over-relaxation parameter for $\bar{v}$ calculation
$\omega_{\bar{w}}$	=	over-relaxation parameter for $\bar{w}$ calculation
ω_{ppp}	=	over-relaxation parameter for ppp calculation
ω_{θ}	=	over-relaxation parameter for θ calculation
Γ	=	system boundary
θ^*	=	temperature
θ^*_r	=	reference temperature
θ^*_h	=	maximum (hot) temperature
θ^*_c	=	minimum (cold) temperature
$\theta_1, \theta_2, \theta_3, \theta_4$	=	coefficients

Subscripts

i	=	grid point counter in the x direction
j	=	grid point counter in the y direction
k	=	grid point counter in the z direction
r	=	grid point counter in the $\bar{x}$ direction
s	=	grid point counter in the $\bar{y}$ direction
t	=	grid point counter in the $\bar{z}$ direction

Superscripts

m	=	dummy time index for counting iterations
n	=	time index

Non-dimensional numbers

Ra	=	Rayleigh number
Re	=	Reynolds number
Pr	=	Prandtl number
Nu	=	Nusselt number

Note: The symbols defined above are subject to alteration on occasion

International Journal for Numerical Methods for Heat & Fluid Flow
Vol. 7 No. 4, 1997, pp. 297-343.

Introduction

Three-dimensional buoyancy-driven flow phenomena are part of everyday life. The flow of air in a building, the heating and cooling of electronic equipment by natural and forced convection and the heating of bottled products for pasteurization are only a few examples of how three-dimensional flows are manipulated. Nevertheless, accurate simulation of these problems is desired in order to obtain quantitative and qualitative information which can then be used to improve and even maximize the effectiveness of the processes that these flows regulate. This is no simple task, owing not only to the complexity of both the equations and the domains in question, but also to computational time limitations. However, the implementation of finite difference schemes for the solution of the pertaining partial differential equations has proven successful now and in the past.

Buoyancy-driven flows, especially in two dimensions, have been the object of thorough study for over 50 years. Owing to the nature of these partial differential equations, most studies in the past have dealt with simplified rectangular domains with different aspect ratios. Nevertheless, without a rigorous, accurate and well understood numerical solution, there was no real way of comparing different numerical schemes in terms of their accuracy, and no way of validating their solutions.

In 1983, de Vahl Davis[1] presented a study which became a benchmark solution for the basic problem of a square cavity (1:1 ratio of height and width) which is heated from the left, cooled on the right and insulated on its top and bottom boundaries. He used the stream-vorticity formulation of the governing equations. Today, there are a few other benchmark solutions available, such as that by Saitoh and Hirose[2]. These solutions are now used as validation tools for both old and new schemes and solutions. Most present computational fluid dynamic studies of buoyant-driven flows use this benchmark problem as their test problem.

With the accelerated rate at which computer speed has increased in the past 30 years and the drop in the cost of performing computations[3], problems that could not be solved years ago are now within our grasp. One such area deals with the study of three-dimensional fluid dynamic problems, and in particular with Navier-Stokes flows in three dimensions. We have been involved in the study of the confined flow of a laminar, incompressible and viscous fluid which is subjected to differential heating and is characterized by two dimensionless parameters: the Rayleigh number and the Prandtl number. In the study the Prandtl number is 1 and the Rayleigh number is varied from 10^3 to 10^6. This involves the solution of the coupled momentum, energy and continuity equations for a fluid. Our goal is to show that the available computer resources are sufficient for the solution of simple and complex three-dimensional problems, that the use of iterative schemes in three dimensions is easy to implement, and that with careful tracking of the problem variables these schemes can generate fast and accurate solutions. To accomplish these goals,

we have duplicated and extended several two-dimensional studies into three dimensions.

We have implemented the fractional step method or projection method proposed by Chorin[4]. Using such an approach we are able to solve the governing equations in their primitive variable form, obtain an explicit formulation for the pressure together with valid boundary conditions for it, and march accurately through time. The pressure calculations are initially done at the centre of the mesh cells, but it is later distributed to the mesh nodes in order to correct the fluid velocities at those points.

In order to solve for the unknowns, we identified about a dozen possible solution algorithms[3,5]. We chose to use the point succesive over-relaxation (PSOR) scheme because, using a first-order accurate finite difference in time as did Fortin[4], the fractional step method transforms the hyperbolic governing equations over time into elliptic equations at every time step. The PSOR scheme is efficient in the solution of elliptic partial differential equations and it is relatively easy to implement in the computer. It is also very flexible in terms of the required accuracy, which can be controlled by changing the tolerance of the iterative solver.

Mathematical model and numerical algorithms

Problem formulation and governing equations

In the current study, the fluid in question is considered to be incompressible and viscous, the flow is laminar, and the domain is three dimensional (3D). To examine the fluid flow, we will solve the unsteady Navier-Stokes equations coupled with the energy equation, all in their primitive variable (u-v-w-p-θ) form. In this formulation u, v and w represent the fluid velocities in the x, y and z directions respectively, while p and θ represent pressure and temperature in that order. This approach was selected over the streamline-vorticity approach owing to the fact that the primitive variable introduces unknowns that are directly observable in real-life systems.

A three-dimensional volume is discretized by a regular mesh with spacings of length Δx, Δy and Δz such that the number of grid points in the x, y and z directions is N_x, N_y and N_z, respectively. The length of the cavity in the x direction is L, the length of the cavity in the y direction is H, and the length in the z direction is W.

By introducing a reference velocity

$$U = \frac{\alpha}{H} \tag{1}$$

the set of non-dimensional variables

$$u = \frac{u^*}{U} \quad v = \frac{v^*}{U} \quad w = \frac{w^*}{U} \tag{2}$$

$$\theta = \frac{(\theta^* - \theta_r^*)}{(\theta_h^* - \theta_c^*)} \tag{3}$$

$$x = \frac{x^*}{H} \quad y = \frac{y^*}{H} \quad z = \frac{z^*}{H} \tag{4}$$

$$p = \frac{p^*}{\rho U^2} \tag{5}$$

$$t = \frac{t^* \alpha}{H^2} \tag{6}$$

is generated, as well as the set of dimensionless parameters

$$Ra = \frac{\rho \bar{\beta} g(\theta_h^* - \theta_c^*) H^3}{\mu \alpha} \tag{7}$$

$$Re = \frac{UH}{\nu} \tag{8}$$

$$Pr = \frac{\nu}{\alpha} \tag{9}$$

Given these, we can write the momentum, energy and conservation of mass equations as

$$a\frac{\partial u}{\partial t} + b\left(u\frac{\partial u}{\partial x} + v\frac{\partial u}{\partial y} + w\frac{\partial u}{\partial z}\right) = -\frac{\partial p}{\partial x} + c\left(\frac{\partial^2 u}{\partial x^2} + \frac{\partial^2 u}{\partial y^2} + \frac{\partial^2 u}{\partial z^2}\right) \tag{10}$$

$$a\frac{\partial v}{\partial t} + b\left(u\frac{\partial v}{\partial x} + v\frac{\partial v}{\partial y} + w\frac{\partial v}{\partial z}\right) = -\frac{\partial p}{\partial y} + c\left(\frac{\partial^2 v}{\partial x^2} + \frac{\partial^2 v}{\partial y^2} + \frac{\partial^2 v}{\partial z^2}\right) + s\theta \tag{11}$$

$$a\frac{\partial w}{\partial t} + b\left(u\frac{\partial w}{\partial x} + v\frac{\partial w}{\partial y} + w\frac{\partial w}{\partial z}\right) = -\frac{\partial p}{\partial z} + c\left(\frac{\partial^2 w}{\partial x^2} + \frac{\partial^2 w}{\partial y^2} + \frac{\partial^2 w}{\partial z^2}\right) \tag{12}$$

$$f\frac{\partial \theta}{\partial t} + d\left(u\frac{\partial \theta}{\partial x} + v\frac{\partial \theta}{\partial y} + w\frac{\partial \theta}{\partial z}\right) = e\left(\frac{\partial^2 \theta}{\partial x^2} + \frac{\partial^2 \theta}{\partial y^2} + \frac{\partial^2 \theta}{\partial z^2}\right) \tag{13}$$

$$\frac{\partial u}{\partial x} + \frac{\partial v}{\partial y} + \frac{\partial w}{\partial z} = 0 \tag{14}$$

where, in our study,

$$a = 1 \quad b = 1 \quad c = Pr \quad d = 1 \quad e = 1 \quad f = 1 \quad s = RaPr \tag{15}$$

As we can observe from the equations, there is no explicit formulation for the pressure. This is one of the reasons why the primitive variable formulation is sometimes avoided. In addition, there is no explicit information available about

the initial pressure profile or the pressure boundary conditions. The non-dimensional form of these equations has been used extensively in the literature[6,7].

Space and time discretization

In order to solve the set of coupled PDEs that describe the problems we are to investigate we will use a finite difference approach. In addition, we will transform the equations using the fractional step method such that we obtain an explicit equation for the pressure. In the fractional step method, a set of intermediate velocities $\bar{u}$, $\bar{v}$ and $\bar{w}$ are introduced such that they are independent from the pressure gradients. In step 1, the fractional step method entails introducing these intermediate velocities into the governing equations, therefore decoupling them from the pressure. The intermediate velocities do not, in general, satisfy the continuity constraint. In step 2, pressure equations are introduced and used in order to obtain real velocities from the intermediate ones. Hence in this scheme, the pressure can be interpreted as an operator which projects the intermediate velocities into divergence-free space where the continuity constraint is satisfied. In terms of the approximation of the derivatives in the governing equations, the selected finite difference approach involves central differencing in the advective and convective terms of the equations, and forward differencing in time. This process yields a set of finite difference equations as follows:

Step 1: *x*-momentum without pressure term:

$$a\frac{\partial u}{\partial t} + b\left(u\frac{\partial u}{\partial x} + v\frac{\partial u}{\partial y} + w\frac{\partial u}{\partial z}\right) = c\left(\frac{\partial^2 u}{\partial x^2} + \frac{\partial^2 u}{\partial y^2} + \frac{\partial^2 u}{\partial z^2}\right) \tag{16}$$

$$a\frac{\bar{u}^{n+1}_{i,j,k} - u^n_{i,j,k}}{\Delta t} + bu\left(\frac{u^n_{i+1,j,k} - u^n_{i-1,j,k}}{2\Delta x}\right) + bv\left(\frac{u^n_{i,j+1,k} - u^n_{i,j-1,k}}{2\Delta y}\right)$$

$$+bw\left(\frac{u^n_{i,j,k+1} - u^n_{i,j,k-1}}{2\Delta z}\right) = c\left(\frac{\bar{u}^{n+1}_{i-1,j,k} - 2\bar{u}^{n+1}_{i,j,k} + \bar{u}^{n+1}_{i+1,j,k}}{\Delta x^2}\right)$$

$$+c\left(\frac{\bar{u}^{n+1}_{i,j-1,k} - 2\bar{u}^{n+1}_{i,j,k} + \bar{u}^{n+1}_{i,j+1,k}}{\Delta y^2}\right) + c\left(\frac{\bar{u}^{n+1}_{i,j,k-1} - 2\bar{u}^{n+1}_{i,j,k} + \bar{u}^{n+1}_{i,j,k+1}}{\Delta z^2}\right) \tag{17}$$

$$\left[\frac{a}{\Delta t} + \frac{2c}{\Delta x^2} + \frac{2c}{\Delta y^2} + \frac{2c}{\Delta z^2}\right]\bar{u}^{n+1}_{i,j,k} + \left[-\frac{c}{\Delta x^2}\right]\bar{u}^{n+1}_{i-1,j,k} + \left[-\frac{c}{\Delta x^2}\right]\bar{u}^{n+1}_{i+1,j,k}$$

$$+\left[-\frac{c}{\Delta y^2}\right]\bar{u}^{n+1}_{i,j-1,k}+\left[-\frac{c}{\Delta y^2}\right]\bar{u}^{n+1}_{i,j+1,k}+\left[-\frac{c}{\Delta z^2}\right]\bar{u}^{n+1}_{i,j,k-1}+\left[-\frac{c}{\Delta z^2}\right]\bar{u}^{n+1}_{i,j,k+1}$$

$$=\left[\frac{a}{\Delta t}\right]u^n_{i,j,k}+\left[-\frac{b}{2\Delta x}\right]\left[\left(u^n_{i,j,k}\right)\left(u^n_{i+1,j,k}\right)-\left(u^n_{i,j,k}\right)\left(u^n_{i-1,j,k}\right)\right]$$

$$+\left[-\frac{b}{2\Delta y}\right]\left[\left(v^n_{i,j,k}\right)\left(u^n_{i,j+1,k}\right)-\left(v^n_{i,j,k}\right)\left(u^n_{i,j-1,k}\right)\right]$$

$$+\left[-\frac{b}{2\Delta z}\right]\left[\left(w^n_{i,j,k}\right)\left(u^n_{i,j,k+1}\right)-\left(w^n_{i,j,k}\right)\left(u^n_{i,j,k-1}\right)\right] \tag{18}$$

y momentum without pressure term:

$$a\frac{\partial v}{\partial t}+b\left(u\frac{\partial v}{\partial x}+v\frac{\partial v}{\partial y}+w\frac{\partial v}{\partial z}\right)=c\left(\frac{\partial^2 v}{\partial x^2}+\frac{\partial^2 v}{\partial y^2}+\frac{\partial^2 v}{\partial z^2}\right)+s\theta \tag{19}$$

$$a\frac{\bar{v}^{n+1}_{i,j,k}-v^n_{i,j,k}}{\Delta t}+bu\left(\frac{v^n_{i+1,j,k}-v^n_{i-1,j,k}}{2\Delta x}\right)+bv\left(\frac{v^n_{i,j+1,k}-v^n_{i,j-1,k}}{2\Delta y}\right)$$

$$+bw\left(\frac{v^n_{i,j,k+1}-v^n_{i,j,k-1}}{2\Delta z}\right)=c\left(\frac{\bar{v}^{n+1}_{i-1,j,k}-2\bar{v}^{n+1}_{i,j,k}+\bar{v}^{n+1}_{i+1,j,k}}{\Delta x^2}\right)$$

$$+c\left(\frac{\bar{v}^{n+1}_{i,j-1,k}-2\bar{v}^{n+1}_{i,j,k}+\bar{v}^{n+1}_{i,j+1,k}}{\Delta y^2}\right)+c\left(\frac{\bar{v}^{n+1}_{i,j,k-1}-2\bar{v}^{n+1}_{i,j,k}+\bar{v}^{n+1}_{i,j,k+1}}{\Delta z^2}\right)+s\theta^n_{i,j,k} \tag{20}$$

$$\left[\frac{a}{\Delta t}+\frac{2c}{\Delta x^2}+\frac{2c}{\Delta y^2}+\frac{2c}{\Delta z^2}\right]\bar{v}^{n+1}_{i,j,k}+\left[-\frac{c}{\Delta x^2}\right]\bar{v}^{n+1}_{i-1,j,k}+\left[-\frac{c}{\Delta x^2}\right]\bar{v}^{n+1}_{i+1,j,k}$$

$$+\left[-\frac{c}{\Delta y^2}\right]\bar{v}^{n+1}_{i,j-1,k}+\left[-\frac{c}{\Delta y^2}\right]\bar{v}^{n+1}_{i,j+1,k}+\left[-\frac{c}{\Delta z^2}\right]\bar{v}^{n+1}_{i,j,k-1}+\left[-\frac{c}{\Delta z^2}\right]\bar{v}^{n+1}_{i,j,k+1}$$

$$=\left[\frac{a}{\Delta t}\right]v^n_{i,j,k}+\left[-\frac{b}{2\Delta x}\right]\left[\left(u^n_{i,j,k}\right)\left(v^n_{i+1,j,k}\right)-\left(u^n_{i,j,k}\right)\left(v^n_{i-1,j,k}\right)\right]$$

$$+\left[-\frac{b}{2\Delta y}\right]\left[\left(v^n_{i,j,k}\right)\left(v^n_{i,j+1,k}\right)-\left(v^n_{i,j,k}\right)\left(v^n_{i,j-1,k}\right)\right]$$

$$+\left[-\frac{b}{2\Delta z}\right]\left[\left(w^n_{i,j,k}\right)\left(v^n_{i,j,k+1}\right)-\left(w^n_{i,j,k}\right)\left(v^n_{i,j,k-1}\right)\right]+s\theta^n_{i,j,k} \tag{21}$$

z momentum without pressure term:

$$a\frac{\partial w}{\partial t}+b\left(u\frac{\partial w}{\partial x}+v\frac{\partial w}{\partial y}+w\frac{\partial w}{\partial z}\right)=c\left(\frac{\partial^2 w}{\partial x^2}+\frac{\partial^2 w}{\partial y^2}+\frac{\partial^2 w}{\partial z^2}\right) \tag{22}$$

$$a\frac{\bar{w}^{n+1}_{i,j,k}-w^{n}_{i,j,k}}{\Delta t}+bu\left(\frac{w^{n}_{i+1,j,k}-w^{n}_{i-1,j,k}}{2\Delta x}\right)+bv\left(\frac{w^{n}_{i,j+1,k}-w^{n}_{i,j-1,k}}{2\Delta y}\right)$$

$$+bw\left(\frac{w^{n}_{i,j,k+1}-w^{n}_{i,j,k-1}}{2\Delta z}\right)=c\left(\frac{\bar{w}^{n+1}_{i-1,j,k}-2\bar{w}^{n+1}_{i,j,k}+\bar{w}^{n+1}_{i+1,j,k}}{\Delta x^2}\right)$$

$$+c\left(\frac{\bar{w}^{n+1}_{i,j-1,k}-2\bar{w}^{n+1}_{i,j,k}+\bar{w}^{n+1}_{i,j+1,k}}{\Delta y^2}\right)+c\left(\frac{\bar{w}^{n+1}_{i,j,k-1}-2\bar{w}^{n+1}_{i,j,k}+\bar{w}^{n+1}_{i,j,k+1}}{\Delta z^2}\right) \tag{23}$$

$$\left[\frac{a}{\Delta t}+\frac{2c}{\Delta x^2}+\frac{2c}{\Delta y^2}+\frac{2c}{\Delta z^2}\right]\bar{w}^{n+1}_{i,j,k}+\left[-\frac{c}{\Delta x^2}\right]\bar{w}^{n+1}_{i-1,j,k}+\left[-\frac{c}{\Delta x^2}\right]\bar{w}^{n+1}_{i+1,j,k}$$

$$+\left[-\frac{c}{\Delta y^2}\right]\bar{w}^{n+1}_{i,j-1,k}+\left[-\frac{c}{\Delta y^2}\right]\bar{w}^{n+1}_{i,j+1,k}+\left[-\frac{c}{\Delta z^2}\right]\bar{w}^{n+1}_{i,j,k-1}+\left[-\frac{c}{\Delta z^2}\right]\bar{w}^{n+1}_{i,j,k+1}$$

$$=\left[\frac{a}{\Delta t}\right]w^{n}_{i,j,k}+\left[-\frac{b}{2\Delta x}\right]\left[\left(u^{n}_{i,j,k}\right)\left(w^{n}_{i+1,j,k}\right)-\left(u^{n}_{i,j,k}\right)\left(w^{n}_{i-1,j,k}\right)\right]$$

$$+\left[-\frac{b}{2\Delta y}\right]\left[\left(v^{n}_{i,j,k}\right)\left(w^{n}_{i,j+1,k}\right)-\left(v^{n}_{i,j,k}\right)\left(w^{n}_{i,j-1,k}\right)\right]$$

$$+\left[-\frac{b}{2\Delta z}\right]\left[\left(w^{n}_{i,j,k}\right)\left(w^{n}_{i,j,k+1}\right)-\left(w^{n}_{i,j,k}\right)\left(w^{n}_{i,j,k-1}\right)\right] \tag{24}$$

Step 2: pressure equation and velocity correctors:
u velocity corrector:

$$a\frac{\partial u}{\partial t}=-\frac{\partial p}{\partial x} \tag{25}$$

$$a\frac{u^{n+1}_{i,j,k}-\bar{u}^{n+1}_{i,j,k}}{\Delta t}=-\left(\frac{\partial p}{\partial x}\right)^{n+1} \tag{26}$$

$$u^{n+1}_{i,j,k}=\bar{u}^{n+1}_{i,j,k}-\left[\frac{\Delta t}{2a\Delta x}\right]\left(p^{n+1}_{i+1,j,k}-p^{n+1}_{i-1,j,k}\right) \tag{27}$$

Partial derivative of equation (25) with respect to *x*:

$$\frac{\partial u_{i,j,k}^{n+1}}{\partial x} = \frac{\partial \bar{u}_{i,j,k}^{n+1}}{\partial x} - \left[\frac{\Delta t}{a}\right]\left(\frac{\partial^2 p}{\partial x^2}\right)^{n+1} \tag{28}$$

v velocity corrector:

$$a\frac{\partial v}{\partial t} = -\frac{\partial p}{\partial y} \tag{29}$$

$$a\frac{v_{i,j,k}^{n+1} - \bar{v}_{i,j,k}^{n+1}}{\Delta t} = -\left(\frac{\partial p}{\partial y}\right)^{n+1} \tag{30}$$

$$v_{i,j,k}^{n+1} = \bar{v}_{i,j,k}^{n+1} - \left[\frac{\Delta t}{2a\Delta y}\right]\left(p_{i,j+1,k}^{n+1} - p_{i,j-1,k}^{n+1}\right) \tag{31}$$

Partial derivative of equation (29) with respect to *y*:

$$\frac{\partial v_{i,j,k}^{n+1}}{\partial y} = \frac{\partial \bar{v}_{i,j,k}^{n+1}}{\partial y} - \left[\frac{\Delta t}{a}\right]\left(\frac{\partial^2 p}{\partial y^2}\right)^{n+1} \tag{32}$$

w velocity corrector:

$$a\frac{\partial w}{\partial t} = -\frac{\partial p}{\partial z} \tag{33}$$

$$a\frac{w_{i,j,k}^{n+1} - \bar{w}_{i,j,k}^{n+1}}{\Delta t} = -\left(\frac{\partial p}{\partial z}\right)^{n+1} \tag{34}$$

$$w_{i,j,k}^{n+1} = \bar{w}_{i,j,k}^{n+1} - \left[\frac{\Delta t}{2a\Delta z}\right]\left(p_{i,j,k+1}^{n+1} - p_{i,j,k-1}^{n+1}\right) \tag{35}$$

Partial derivative of equation (33) with respect to *z*:

$$\frac{\partial w_{i,j,k}^{n+1}}{\partial z} = \frac{\partial \bar{w}_{i,j,k}^{n+1}}{\partial z} - \left[\frac{\Delta t}{a}\right]\left(\frac{\partial^2 p}{\partial z^2}\right)^{n+1} \tag{36}$$

Adding up equations (28), (32) and (36) yields

$$\left(\frac{\partial u_{i,j,k}^{n+1}}{\partial x} + \frac{\partial v_{i,j,k}^{n+1}}{\partial y} + \frac{\partial w_{i,j,k}^{n+1}}{\partial z}\right) = \left(\frac{\partial \bar{u}_{i,j,k}^{n+1}}{\partial x} + \frac{\partial \bar{v}_{i,j,k}^{n+1}}{\partial y} + \frac{\partial \bar{w}_{i,j,k}^{n+1}}{\partial z}\right)$$

$$-\left[\frac{\Delta t}{a}\right]\left(\frac{\partial^2 p^{n+1}}{\partial x^2} + \frac{\partial^2 p^{n+1}}{\partial y^2} + \frac{\partial^2 p^{n+1}}{\partial z^2}\right) \tag{37}$$

As one can see, the left-hand side of equation (37) is the same as equation (14), i.e. a statement of conservation of mass, and is therefore equal to zero, such that we are left with

$$\left(\frac{\partial^2 p^{n+1}}{\partial x^2}+\frac{\partial^2 p^{n+1}}{\partial y^2}+\frac{\partial^2 p^{n+1}}{\partial z^2}\right)=\left[\frac{a}{\Delta t}\right]\left(\frac{\partial \bar{u}^{n+1}_{i,j,k}}{\partial x}+\frac{\partial \bar{v}^{n+1}_{i,j,k}}{\partial y}+\frac{\partial \bar{w}^{n+1}_{i,j,k}}{\partial z}\right) \tag{38}$$

because, in general, the intermediate velocities do not satisfy the conservation of mass equation (i.e. they are not divergence-free).

Equations (27), (31) and (35) are used to correct the intermediate velocities $\bar{u}$, $\bar{v}$ and $\bar{w}$ into u, v and w respectively, after the pressure has been updated by solving equation (38).

Step 3: energy equation

$$f\frac{\partial\theta}{\partial t}+d\left(u\frac{\partial\theta}{\partial x}+v\frac{\partial\theta}{\partial y}+w\frac{\partial\theta}{\partial z}\right)=e\left(\frac{\partial^2\theta}{\partial x^2}+\frac{\partial^2\theta}{\partial y^2}+\frac{\partial^2\theta}{\partial z^2}\right) \tag{39}$$

$$f\frac{\bar{\theta}^{n+1}_{i,j,k}-\theta^{n}_{i,j,k}}{\Delta t}+du\left(\frac{\theta^{n}_{i+1,j,k}-\theta^{n}_{i-1,j,k}}{2\Delta x}\right)+dv\left(\frac{\theta^{n}_{i,j+1,k}-\theta^{n}_{i,j-1,k}}{2\Delta y}\right) \tag{40}$$

$$+dw\left(\frac{\theta^{n}_{i,j,k+1}-\theta^{n}_{i,j,k-1}}{2\Delta z}\right)=e\left(\frac{\bar{\theta}^{n+1}_{i-1,j,k}-2\bar{\theta}^{n+1}_{i,j,k}+\bar{\theta}^{n+1}_{i+1,j,k}}{\Delta x^2}\right)$$

$$+e\left(\frac{\bar{\theta}^{n+1}_{i,j-1,k}-2\bar{\theta}^{n+1}_{i,j,k}+\bar{\theta}^{n+1}_{i,j+1,k}}{\Delta y^2}\right)+e\left(\frac{\bar{\theta}^{n+1}_{i,j,k-1}-2\bar{\theta}^{n+1}_{i,j,k}+\bar{\theta}^{n+1}_{i,j,k+1}}{\Delta z^2}\right)$$

$$\left[\frac{f}{\Delta t}+\frac{2e}{\Delta x^2}+\frac{2e}{\Delta y^2}+\frac{2e}{\Delta z^2}\right]\bar{\theta}^{n+1}_{i,j,k}+\left[-\frac{e}{\Delta x^2}\right]\bar{\theta}^{n+1}_{i-1,j,k}+\left[-\frac{e}{\Delta x^2}\right]\bar{\theta}^{n+1}_{i+1,j,k}$$

$$+\left[-\frac{e}{\Delta y^2}\right]\bar{\theta}^{n+1}_{i,j-1,k}+\left[-\frac{e}{\Delta y^2}\right]\bar{\theta}^{n+1}_{i,j+1,k}+\left[-\frac{e}{\Delta z^2}\right]\bar{\theta}^{n+1}_{i,j,k-1}+\left[-\frac{e}{\Delta z^2}\right]\bar{\theta}^{n+1}_{i,j,k+1}$$

$$=\left[\frac{f}{\Delta t}\right]\theta^{n}_{i,j,k}+\left[-\frac{d}{2\Delta x}\right]\left[\left(u^{n}_{i,j,k}\right)\left(\theta^{n}_{i+1,j,k}\right)-\left(u^{n}_{i,j,k}\right)\left(\theta^{n}_{i-1,j,k}\right)\right]$$

$$+\left[-\frac{d}{2\Delta y}\right]\left[\left(v^{n}_{i,j,k}\right)\left(\theta^{n}_{i,j+1,k}\right)-\left(v^{n}_{i,j,k}\right)\left(\theta^{n}_{i,j-1,k}\right)\right]$$

$$+\left[-\frac{d}{2\Delta z}\right]\left[\left(w^{n}_{i,j,k}\right)\left(\theta^{n}_{i,j,k+1}\right)-\left(w^{n}_{i,j,k}\right)\left(\theta^{n}_{i,j,k-1}\right)\right] \tag{41}$$

So, equations (18), (21), (24), (38) and (41), together with the correction equations mentioned previously, are the finite difference representation of the governing equations.

Treatment of the pressure

Because the finite difference formulation used is second-order in x, y and z, and first-order in time, the system behaves well for a large range of Rayleigh numbers. We have solved benchmark problems as well as a series of problems in 3D that include both Dirichlet and Neumann boundary conditions, as well as problems with complex, multi-body geometries. Nevertheless, because the problems do not give direct information about the pressure, such information has to be deduced in other ways. Based on the projection method proposed by Chorin[4], which is in fact the fractional step method with a first-order formulation in time, a Neumann condition for the pressure is obtained of the form:

$$\left(\frac{\partial p}{\partial N}\right)_{\Gamma}^{n+1} = -\frac{1}{\Delta t}\left(U_{\Gamma}^{n+1} - \tilde{U}_{\Gamma}\right) \cdot N \tag{42}$$

where N is the vector of directions [x y z] and U is the vector of velocities [u v w]. In all the problems presented in this study, the velocities in question are specified at the boundaries, leading to the conclusion that the pressure flux in any direction at the boundaries is zero.

We limit our work to regular meshes with parallelepiped cells. For that reason there are nodes, such as the corners of the cavities studied, at which the given pressure information is not helpful. Our solution is to transform equation (38) such that the solution scheme is applied to the pressure at the centre of the mesh cells, yielding a value *ppp*. Then, *ppp* is distributed back to the mesh nodes in order to obtain p at all points, including the cavity corners. Our solution of the benchmark problem suggests that our approach is not only valid but also accurate.

We start by creating a new mesh system based on the centre of the cells of the original grid. Therefore, the number of grid points in the $\bar{x}$, $\bar{y}$ and $\bar{z}$ directions is $N_{\bar{x}}$, $N_{\bar{y}}$ and $N_{\bar{z}}$, where $N_{\bar{x}} = N_x - 1$, $N_{\bar{y}} = N_y - 1$ and $N_{\bar{z}} = N_z - 1$. We want to solve equation (38) in the new grid system. Figure 1 shows the nodes of the original system as well as the nodes of the new one. In the new grid space $\bar{x}$-$\bar{y}$-$\bar{z}$ we count the nodes in $\bar{x}$ with r, the nodes in $\bar{y}$ with s and the nodes in $\bar{z}$ with t. Remember, in the original space x-y-z we count the nodes in x with i, the nodes in y with j and the nodes in z with k. So if we apply a finite difference formulation to equation (38) in the new grid system we obtain

$$\begin{aligned}
&\left(\frac{ppp_{r+1,s,t} - 2ppp_{r,s,t} + ppp_{r-1,s,t}}{\Delta x^2}\right) + \left(\frac{ppp_{r,s+1,t} - 2ppp_{r,s,t} + ppp_{r,s-1,t}}{\Delta y^2}\right) \\
&+ \left(\frac{ppp_{r,s,t+1} - 2ppp_{r,s,t} + ppp_{r,s,t-1}}{\Delta z^2}\right) = \left[\frac{a}{\Delta t}\right]\left(\frac{\bar{u}_{r+\frac{1}{2},s,t} - \bar{u}_{r-\frac{1}{2},s,t}}{\Delta x}\right) \\
&+ \left[\frac{a}{\Delta t}\right]\left(\frac{\bar{v}_{r,s+\frac{1}{2},t} - \bar{v}_{r,s-\frac{1}{2},t}}{\Delta y}\right) + \left[\frac{a}{\Delta t}\right]\left(\frac{\bar{w}_{r,s,t+\frac{1}{2}} - \bar{w}_{r,s,t-\frac{1}{2}}}{\Delta z}\right)
\end{aligned} \tag{43}$$

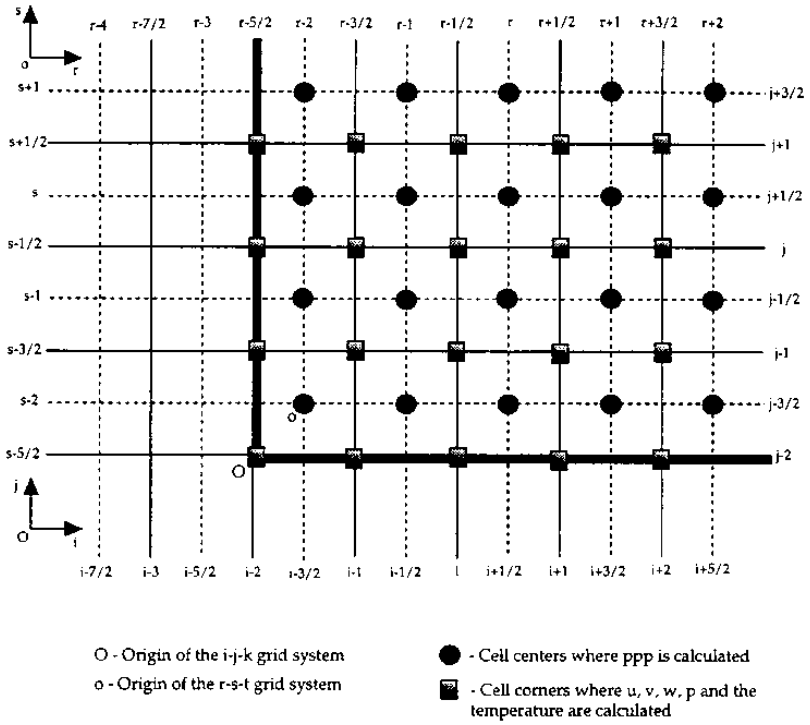

Figure 1.
Two-dimensional projection of the three-dimensional grid system used. Notice that the thick line represents a system boundary

which, in terms of the intermediate velocity values at the nodes of the original grid, becomes

$$\left(\frac{ppp_{r+1,s,t} - 2ppp_{r,s,t} + ppp_{r-1,s,t}}{\Delta x^2}\right) + \left(\frac{ppp_{r,s+1,t} - 2ppp_{r,s,t} + ppp_{r,s-1,t}}{\Delta y^2}\right)$$

$$+ \left(\frac{ppp_{r,s,t+1} - 2ppp_{r,s,t} + ppp_{r,s,t-1}}{\Delta z^2}\right) = \left[\frac{a}{\Delta t}\right]\left(\frac{A-B}{\Delta x}\right)$$

$$+ \left[\frac{a}{\Delta t}\right]\left(\frac{C-D}{\Delta y}\right) + \left[\frac{a}{\Delta t}\right]\left(\frac{E-F}{\Delta z}\right) \tag{44}$$

where

$$A = \bar{u}_{i+1,j+\frac{1}{2},k+\frac{1}{2}} = \left(\frac{1}{2}\right)\left(\bar{u}_{i+1,j,k+\frac{1}{2}} + \bar{u}_{i+1,j+1,k+\frac{1}{2}}\right) =$$

$$\left(\frac{1}{4}\right)\left(\bar{u}_{i+1,j,k} + \bar{u}_{i+1,j,k+1}\right) + \left(\frac{1}{4}\right)\left(\bar{u}_{i+1,j+1,k} + \bar{u}_{i+1,j+1,k+1}\right) \tag{45}$$

$$B = \bar{u}_{i,j+\frac{1}{2},k+\frac{1}{2}} = \left(\frac{1}{2}\right)\left(\bar{u}_{i,j,k+\frac{1}{2}} + \bar{u}_{i,j+1,k+\frac{1}{2}}\right) =$$

$$\left(\frac{1}{4}\right)\left(\bar{u}_{i,j,k} + \bar{u}_{i,j,k+1}\right) + \left(\frac{1}{4}\right)\left(\bar{u}_{i,j+1,k} + \bar{u}_{i,j+1,k+1}\right) \tag{46}$$

$$C = \bar{v}_{i+\frac{1}{2},j+1,k+\frac{1}{2}} = \left(\frac{1}{2}\right)\left(\bar{v}_{i,j+1,k+\frac{1}{2}} + \bar{v}_{i+1,j+1,k+\frac{1}{2}}\right) =$$

$$\left(\frac{1}{4}\right)\left(\bar{v}_{i,j+1,k} + \bar{v}_{i,j+1,k+1}\right) + \left(\frac{1}{4}\right)\left(\bar{v}_{i+1,j+1,k} + \bar{v}_{i+1,j+1,k+1}\right) \tag{47}$$

$$D = \bar{v}_{i+\frac{1}{2},j,k+\frac{1}{2}} = \left(\frac{1}{2}\right)\left(\bar{v}_{i,j,k+\frac{1}{2}} + \bar{v}_{i+1,j,k+\frac{1}{2}}\right) =$$

$$\left(\frac{1}{4}\right)\left(\bar{v}_{i,j,k} + \bar{v}_{i,j,k+1}\right) + \left(\frac{1}{4}\right)\left(\bar{v}_{i+1,j,k} + \bar{u}_{i+1,j,k+1}\right) \tag{48}$$

$$E = \bar{w}_{i+\frac{1}{2},j+\frac{1}{2},k+1} = \left(\frac{1}{2}\right)\left(\bar{w}_{i,j+\frac{1}{2},k+1} + \bar{w}_{i+1,j+\frac{1}{2},k+1}\right) =$$

$$\left(\frac{1}{4}\right)\left(\bar{w}_{i,j,k+1} + \bar{w}_{i,j+1,k+1}\right) + \left(\frac{1}{4}\right)\left(\bar{w}_{i+1,j,k+1} + \bar{w}_{i+1,j+1,k+1}\right) \tag{49}$$

$$F = \bar{w}_{i+\frac{1}{2},j+\frac{1}{2},k} = \left(\frac{1}{2}\right)\left(\bar{w}_{i,j+\frac{1}{2},k} + \bar{w}_{i+1,j+\frac{1}{2},k}\right) =$$

$$\left(\frac{1}{4}\right)\left(\bar{w}_{i,j,k} + \bar{w}_{i,j+1,k}\right) + \left(\frac{1}{4}\right)\left(\bar{w}_{i+1,j,k} + \bar{w}_{i+1,j+1,k}\right) \tag{50}$$

Given equation (44), we can solve for the pressure at the centres of the grid cells. Redistributing *ppp* to the nodes of the original mesh is a simple operation governed by the way the mesh cells surround the mesh node in question and the pressure boundary conditions.

Method of solution

Elliptic partial differential equations, when reduced to finite difference equations by using central differencing, generate a set of algebraic equations that can be solved by two major classes of methods. Direct methods rely on solving the matrix problem at hand by Gaussian elimination, Cramer's rule, matrix inversion, lower upper (LU) decomposition or any other similar scheme.

Direct solvers are versatile, but run into trouble as the number of unknowns of the system increases, because the number of operations required to solve it increases very rapidly, and so does the computational time. Nevertheless, there are direct solver algorithms that exploit characteristics of the system of equations to speed up the solution process, such as the conjugate gradient method (CG), but there is a trade-off in terms of the complexity of the computer algorithms and their implementation. The other general class of solution schemes for elliptic equations has been labelled iterative schemes. Iterative schemes include schemes such as the Jacobi method, the Gauss-Seidel method (GS), the line Gauss-Seidel method (LGS), the point successive over-relaxation method (PSOR), the line successive over-relaxation method (LSOR), the alternating direction implicit method (ADI) and others. All of these schemes rely on the same basic strategy, with few changes designed to increase the rate of convergence to the actual solution. The tactic can be described as follows. To start the algorithms, a solution is guessed. The equation is rearranged such that the desired nodal value or values become the unknowns, and the other nodes are moved to the opposite side of the difference equation. A dummy time index m is introduced to represent the current iteration, such that $m + 1$ represents the next one. Then, the unknowns are indexed at the $m + 1$th iteration level, and the knowns are indexed at the mth iteration level. The algorithm scans through the mesh in such a way that, at the end, both a value at the $m + 1$th iteration and at the mth iteration exists for every point in the mesh. Then we define a parameter ε such that

$$\epsilon = \sum_{i=1}^{N_x} \sum_{j=1}^{N_y} \sum_{k=1}^{N_z} ABS\left[X_{i,j,k}^{m+1} - X_{i,j,k}^{m}\right] \tag{51}$$

that is, ε is the sum of all the differences between the value of X at the i, j, kth mesh points at the mth time level, and the value of X at the same mesh point but at the $m + 1$th time level, where X is the unknown quantity in question. The value of ε can be used as a measure of how different two consecutive iterations are. The process of solution is repeated until the value of ε goes below the desired tolerance. At that moment, the latest value of X is the solution.

Why do these schemes converge at all? In general, iterative schemes rewrite spatially discretized time independent elliptic equations in a form indistiguishable from that of spatially and temporally discretized time-dependent parabolic equations. In the case of parabolic equations, their solutions converge to a steady state as real time progresses. Identically, elliptic equations with iterative solvers will also converge to a final state as the number of iterations increases. However, the iteration counter, although time-like, has no physical meaning whatsoever.

The most general version of the iterative schemes is the Jacobi method, which corresponds to the previous description. In our study, the PSOR scheme was selected as the solution scheme. In the PSOR, a parameter, ω, is introduced to accelerate the convergence of the scheme. The optimum value of ω can be

calculated analytically for a very limited number of simple problems and boundary conditions. In general, the optimum value is found experimentally. In addition to this enhancement, the PSOR scheme utilizes the latest updated values as it scans the mesh, that is, as values are updated they are introduced into the formulation, increasing the scheme's performance even more.

In the current study, the PSOR scheme is applied to all the governing equations. There are various reasons for this. First of all, it can be observed that after applying the fractional step method, the equation obtained for the pressure is in fact elliptic, and suited for solution by the PSOR scheme. But what about the other equations? When a forward difference is introduced to deal with the time derivatives, the time-dependent equations become elliptic for any individual time step. Therefore, at every time step, p, θ, $\bar{u}$, $\bar{v}$ and $\bar{w}$ can be solved using the PSOR method. This can reduce the complexity of the computer implementation immensely. The difference equations can be rewritten in PSOR form as follows:

$\bar{u}$ equation:

$$\bar{u}_{i,j,k}^{m+1} = (1-\omega_{\bar{u}})\,\bar{u}_{i,j,k}^{m} + \left(\frac{\omega_{\bar{u}}}{c_{ij}}\right)\left(U_1 + U_2 + U_3 + U_4 - a_{ij}\bar{u}_{i-1,j,k}^{m} - b_{ij}\bar{u}_{i+1,j,k}^{m} - d_{ij}\bar{u}_{i,j-1,k}^{m} - e_{ij}\bar{u}_{i,j+1,k}^{m} - f_{ij}\bar{u}_{i,j,k-1}^{m} - g_{ij}\bar{u}_{i,j,k+1}^{m}\right) \quad (52)$$

where

$$U_1 = -\left(\frac{b}{2\Delta x}\right)(u_{i,j,k}u_{i+1,j,k} - u_{i,j,k}u_{i-1,j,k})$$

$$U_2 = -\left(\frac{b}{2\Delta y}\right)(v_{i,j,k}u_{i,j+1,k} - v_{i,j,k}u_{i,j-1,k})$$

$$U_3 = -\left(\frac{b}{2\Delta z}\right)(w_{i,j,k}u_{i,j,k+1} - w_{i,j,k}u_{i,j,k-1})$$

$$U_4 = \left(\frac{a}{\Delta t}\right)(u_{i,j,k})$$

and

$$a_{ij} = b_{ij} = -\left(\frac{c}{\Delta x^2}\right) \qquad d_{ij} = e_{ij} = -\left(\frac{c}{\Delta y^2}\right) \qquad f_{ij} = g_{ij} = -\left(\frac{c}{\Delta z^2}\right)$$

$$c_{ij} = \left(\frac{a}{\Delta t}\right) + \left(\frac{2c}{\Delta x^2}\right) + \left(\frac{2c}{\Delta y^2}\right) + \left(\frac{2c}{\Delta z^2}\right)$$

$\bar{v}$ equation:

$$\bar{v}_{i,j,k}^{m+1} = (1-\omega_{\bar{v}})\,\bar{v}_{i,j,k}^{m} + \left(\frac{\omega_{\bar{v}}}{c_{ij}}\right)\left(V_1 + V_2 + V_3 + V_4 - a_{ij}\bar{v}_{i-1,j,k}^{m} - b_{ij}\bar{v}_{i+1,j,k}^{m}\right.$$

$$\left. - d_{ij}\bar{v}_{i,j-1,k}^{m} - e_{ij}\bar{v}_{i,j+1,k}^{m} - f_{ij}\bar{v}_{i,j,k-1}^{m} - g_{ij}\bar{v}_{i,j,k+1}^{m} + s\theta_{i,j,k}^{m}\right) \quad (53)$$

where

$$V_1 = -\left(\frac{b}{2\Delta x}\right)(u_{i,j,k}v_{i+1,j,k} - u_{i,j,k}v_{i-1,j,k})$$

$$V_2 = -\left(\frac{b}{2\Delta y}\right)(v_{i,j,k}v_{i,j+1,k} - v_{i,j,k}v_{i,j-1,k})$$

$$V_3 = -\left(\frac{b}{2\Delta z}\right)(w_{i,j,k}v_{i,j,k+1} - w_{i,j,k}v_{i,j,k-1})$$

$$V_4 = \left(\frac{a}{\Delta t}\right)(v_{i,j,k})$$

and

$$a_{ij} = b_{ij} = -\left(\frac{c}{\Delta x^2}\right) \qquad d_{ij} = e_{ij} = -\left(\frac{c}{\Delta y^2}\right) \qquad f_{ij} = g_{ij} = -\left(\frac{c}{\Delta z^2}\right)$$

$$c_{ij} = \left(\frac{a}{\Delta t}\right) + \left(\frac{2c}{\Delta x^2}\right) + \left(\frac{2c}{\Delta y^2}\right) + \left(\frac{2c}{\Delta z^2}\right)$$

$\bar{w}$ equation:

$$\bar{w}_{i,j,k}^{m+1} = (1-\omega_{\bar{w}})\,\bar{w}_{i,j,k}^{m} + \left(\frac{\omega_{\bar{w}}}{c_{ij}}\right)\left(W_1 + W_2 + W_3 + W_4 - a_{ij}\bar{w}_{i-1,j,k}^{m}\right.$$

$$\left. - b_{ij}\bar{w}_{i+1,j,k}^{m} - d_{ij}\bar{w}_{i,j-1,k}^{m} - e_{ij}\bar{w}_{i,j+1,k}^{m} - f_{ij}\bar{w}_{i,j,k-1}^{m} - g_{ij}\bar{w}_{i,j,k+1}^{m}\right) \quad (54)$$

where

$$W_1 = -\left(\frac{b}{2\Delta x}\right)(u_{i,j,k}w_{i+1,j,k} - u_{i,j,k}w_{i-1,j,k})$$

$$W_2 = -\left(\frac{b}{2\Delta y}\right)(v_{i,j,k}w_{i,j+1,k} - v_{i,j,k}w_{i,j-1,k})$$

$$W_3 = -\left(\frac{b}{2\Delta z}\right)(w_{i,j,k}w_{i,j,k+1} - w_{i,j,k}w_{i,j,k-1})$$

$$W_4 = \left(\frac{a}{\Delta t}\right)(w_{i,j,k})$$

and

$$a_{ij} = b_{ij} = -\left(\frac{c}{\Delta x^2}\right) \quad d_{ij} = e_{ij} = -\left(\frac{c}{\Delta y^2}\right) \quad f_{ij} = g_{ij} = -\left(\frac{c}{\Delta z^2}\right)$$

$$c_{ij} = \left(\frac{a}{\Delta t}\right) + \left(\frac{2c}{\Delta x^2}\right) + \left(\frac{2c}{\Delta y^2}\right) + \left(\frac{2c}{\Delta z^2}\right)$$

ppp equation:

$$ppp_{i,j,k}^{m+1} = (1 - \omega_{ppp})\, ppp_{i,j,k}^{m} + \left(\frac{\omega_{ppp}}{c_{ij}}\right)\left(-a_{ij}ppp_{i-1,j,k}^{m} - b_{ij}ppp_{i+1,j,k}^{m}\right.$$

$$\left. - d_{ij}ppp_{i,j-1,k}^{m} - e_{ij}ppp_{i,j+1,k}^{m} - f_{ij}ppp_{i,j,k-1}^{m} - g_{ij}ppp_{i,j,k+1}^{m} + G\right) \qquad (55)$$

where

$$a_{ij} = b_{ij} = \left(\frac{1}{\Delta x^2}\right) \quad d_{ij} = e_{ij} = \left(\frac{1}{\Delta y^2}\right) \quad f_{ij} = g_{ij} = \left(\frac{1}{\Delta z^2}\right)$$

$$c_{ij} = \left(\frac{-2}{\Delta x^2} + \frac{-2}{\Delta y^2} + \frac{-2}{\Delta z^2}\right)$$

where

$$G = \left(\frac{a}{\Delta t}\right)\left(\frac{A - B}{\Delta x} + \frac{C - D}{\Delta y} + \frac{E - F}{\Delta z}\right)$$

while *A*, *B*, *C*, *D*, *E* and *F* are given by equations (45) through (50) respectively.
θ equation:

$$\theta_{i,j,k}^{m+1} = (1-\omega_\theta)\,\theta_{i,j,k}^{m} + \left(\frac{\omega_\theta}{c_{ij}}\right)\left(\theta_1+\theta_2+\theta_3+\theta_4 - a_{ij}\theta_{i-1,j,k}^{m} - b_{ij}\theta_{i+1,j,k}^{m}\right.$$

$$\left. - d_{ij}\theta_{i,j-1,k}^{m} - e_{ij}\theta_{i,j+1,k}^{m} - f_{ij}\theta_{i,j,k-1}^{m} - g_{ij}\theta_{i,j,k+1}^{m}\right) \tag{56}$$

where

$$\theta_1 = -\left(\frac{d}{2\Delta x}\right)(u_{i,j,k}\theta_{i+1,j,k} - u_{i,j,k}\theta_{i-1,j,k})$$

$$\theta_2 = -\left(\frac{d}{2\Delta y}\right)(v_{i,j,k}\theta_{i,j+1,k} - v_{i,j,k}\theta_{i,j-1,k})$$

$$\theta_3 = -\left(\frac{d}{2\Delta z}\right)(w_{i,j,k}\theta_{i,j,k+1} - w_{i,j,k}\theta_{i,j,k-1})$$

$$\theta_4 = \left(\frac{f}{\Delta t}\right)(\theta_{i,j,k})$$

and

$$a_{ij} = b_{ij} = -\left(\frac{e}{\Delta x^2}\right) \qquad d_{ij} = e_{ij} = -\left(\frac{e}{\Delta y^2}\right) \qquad f_{ij} = g_{ij} = -\left(\frac{e}{\Delta z^2}\right)$$

$$c_{ij} = \left(\frac{f}{\Delta t}\right) + \left(\frac{2e}{\Delta x^2}\right) + \left(\frac{2e}{\Delta y^2}\right) + \left(\frac{2e}{\Delta z^2}\right)$$

Benchmark problem: thermally-driven cavity

One classic problem described by the governing equations is the buoyancy-driven flow of a viscous fluid in a unit square enclosure. This two-dimensional problem is used as a benchmark and code validation tool owing to the existence of very accurate and complete studies such as those by de Vahl Davis[1] and Saitoh and Hirose[2]. Figure 2 is a three-dimensional representation of the geometry of the problem.

The boundary conditions of the two-dimensional benchmark are

$$u(0,y,t) = 0, \qquad v(0,y,t) = 0, \qquad \theta(0,y,t) = 0.5, \qquad \frac{\partial p(0,y,t)}{\partial x} = 0 \tag{57}$$

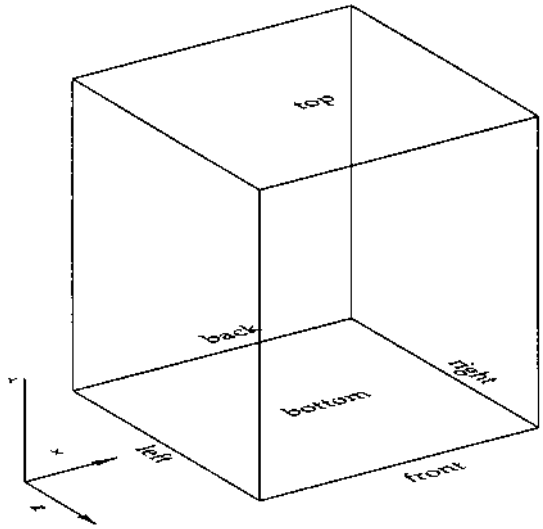

Figure 2.
Geometry for the benchmark problem where a unit cube cavity is heated from the left, cooled from the right, and insulated on the top, bottom, front and back walls

$$u(1,y,t)=0. \quad v(1,y.t)=0, \quad \theta(1,y,t)=-0.5, \quad \frac{\partial p(1,y,t)}{\partial x}=0 \tag{58}$$

$$u(x,0,t)=0, \quad v(x,0,t)=0, \quad \frac{\partial \theta(x,0,t)}{\partial y}=0, \quad \frac{\partial p(x,0,t)}{\partial y}=0 \tag{59}$$

$$u(x,1,t)=0, \quad v(x,1,t)=0, \quad \frac{\partial \theta(x,1,t)}{\partial y}=0, \quad \frac{\partial p(x,1,t)}{\partial y}=0 \tag{60}$$

In our study we solve the three-dimensional version of the thermally-driven cavity problem whose boundary conditions can be written as

$$u(0,y,z,t)=0, \quad v(0,y,z,t)=0, \quad w(0,y,z,t)=0,$$

$$\theta(0,y,z,t)=0.5, \quad \frac{\partial p(0,y,z,t)}{\partial x}=0 \tag{61}$$

$$u(1,y,z,t)=0, \quad v(1,y,z,t)=0, \quad w(1,y,z,t)=0,$$

$$\theta(1,y,z,t)=-0.5, \quad \frac{\partial p(1,y,z,t)}{\partial x}=0 \tag{62}$$

$$u(x,0,z,t)=0, \quad v(x,0,z,t)=0, \quad w(x,0,z,t)=0,$$

$$\frac{\partial\theta(x,0,z,t)}{\partial y}=0, \quad \frac{\partial p(x,0,z,t)}{\partial y}=0 \tag{63}$$

$$u(x,1,z,t)=0, \quad v(x,1,z,t)=0, \quad w(x,1,z,t)=0,$$

$$\frac{\partial\theta(x,1,z,t)}{\partial y}=0, \quad \frac{\partial p(x,1,z,t)}{\partial y}=0 \tag{64}$$

$$u(x,y,0,t)=0, \quad v(x,y,0,t)=0, \quad w(x,y,0,t)=0,$$

$$\frac{\partial\theta(x,y,0,t)}{\partial z}=0, \quad \frac{\partial p(x,y,0,t)}{\partial z}=0 \tag{65}$$

$$u(x,y,1,t)=0, \quad v(x,y,1,t)=0, \quad w(x,y,1,t)=0,$$

$$\frac{\partial\theta(x,y,1,t)}{\partial z}=0, \quad \frac{\partial p(x,y,1,t)}{\partial z}=0 \tag{66}$$

The three-dimensional scheme can solve the two-dimensional benchmark when the number of nodes in the z direction is equal to 3. With this many nodes in the z direction, the three-dimensional problem collapses into its two-dimensional counterpart, so it can be validated. Benchmark results available from various sources report results for a $Pr = 0.71$ and a range of Ra from 10^3 to 10^6. We have solved the 2D benchmark for the same Pr and the same Ra range for meshes with 11×11, 21×21, 41×41 and 61×61 grid points. In addition, we have solved the fully three-dimensional problem for $Pr = 0.71$ and Rayleigh numbers ranging from 10^3 to 10^6 in meshes with between $11\times11\times11$ and $41\times41\times17$ grid points.

Two-dimensional problem

In the two-dimensional projection of the unit cube thermally-driven cavity problem, we can examine the effect of the Ra on the flow pattern and the heat flux profile. Owing to the nature of the problem we can expect both Rayleigh number dependent and Rayleigh number independent fluid behaviour.

Both the x momentum and y momentum equations have a common non-linear convective term. The y momentum equation, however, has an extra convective term related to the buoyant force. We call this term the convective buoyant term. The term $s = RaPr$ in the momentum equation (11) is a measure

of how intense the convective buoyant effect is in the fluid system. In addition, the differential heating of the cavity produces a temperature difference between the fluid and the heated right wall, and the fluid and the cooled left wall and, therefore, a heat flux as well. As the $RaPr$ product grows, the same temperature differential applied to the cavity has more influence on the vertical v velocity of the fluid, than on the u velocity. As time progresses and heat is transferred from the walls to the fluid, the vertical and horizontal velocities initiate flow circulation. As the fluid gets hotter near the right wall, the value of θ of the fluid close to the wall becomes positive. This produces a positive convective buoyant term, thus causing a pronounced movement of the fluid against the gravity gradient, in our case, upwards. In a similar manner, the fluid gets colder near the left wall, the value of θ of the fluid close to the wall becomes negative. This produces a negative buoyant term, causing the fluid to move in the direction of the gravity gradient, in our case, downwards. This fluid movement extends throughout the cavity, and therefore we expect a clockwise rotation of the fluid as the system evolves in time. This effect is expected for any Ra, but is, of course, more pronounced for larger Ra.

In order to visualize the conductive and convective effects, temperature contour plots are ideal. In an insulated wall, the heat transfer is purely conductive. We can use the isotherm pattern of such a wall as a reference with which to compare the temperature contours at different cross-sections of the system, so as to assess the changes in the way heat is transferred in the fluid. The isotherms in a purely conductive cross-section have a particular curvature. Deviations from this isotherm pattern indicate changes in the energy transfer mechanisms.

For $Ra = 10^3$, Figure 3a shows that the isotherm pattern is very close to that of an insulated wall. That indicates that heat is being mainly transferred by conduction. This can also be inferred from the flow pattern in Figure 4a. The flow is perfectly symmetric at this Ra, therefore there are no areas in the flow where the velocities are significantly different from the rest. The slight change in the curvature of the isotherms indicates, however, that convection is beginning to have an effect.

For $Ra = 10^4$, the isotherms in Figure 3b show a definite change from pure conduction. The hot and cold isotherms begin to elongate clockwise in the top and the bottom of the cavity, respectively. This indicates that hotter fluid can now be found close to the left and top walls, and cold fluid can be found close to the right and bottom walls, as expected from the fluid circulation. In addition, notice that the isotherms are now closer to each other near the left and right walls. This indicates that the temperature differences at the walls are larger, therefore, the heat flux is now larger than before, also as expected. We therefore expect an increase in the local Nu in the regions where the isotherms are closely packed. The flow pattern has also changed as we can see in Figure 4b. The flow is still symmetric but the streamlines are closer together near the left and right walls, which means that the fluid velocity in the vertical direction is increasing

faster than the horizontal velocity, due to the added effect of the convective buoyant ($s\theta$) term.

For $Ra = 10^5$, Figure 3c shows that the isotherm pattern is an extension of what is observed at 10^4. The isotherms are even closer together at the hot and cold walls, so the heat flux is still increasing, and their curvature indicates that the flow is much more convective. Nevertheless, there is a basic difference between the flow pattern at 10^5 and that at 10^4. As we can observe in Figure 4c, the streamline pattern has decentralized and in fact created two identical circulation cells. The streamline pattern near the heated walls is more closely packed, indicating an increase in v velocity due to the even stronger effect of the Ra. As a final observation, one can see that the isotherm pattern follows the streamline pattern closely, that is, near the new circulation cells, the isotherms are bent to follow the streamlines.

Finally, for $Ra = 10^6$, the isotherm pattern in Figure 3d is extremely bent near the heated walls. The heat flux is very large near the walls, as one can observe from the closeness of the isothermal lines. In terms of the fluid motion, Figure 4d shows that the two cells from the 10^5 case still exist but have elongated in the y direction, and have moved farther apart in the x direction. Notice that the flow circulation at the cells is still not strong enough to create local mixing of fluid, that is, we are not observing folding of the isotherms or formation of more than one rotation cell. Finally, from Figure 5 it is expected that the pressure field is influenced by the cavity corners.

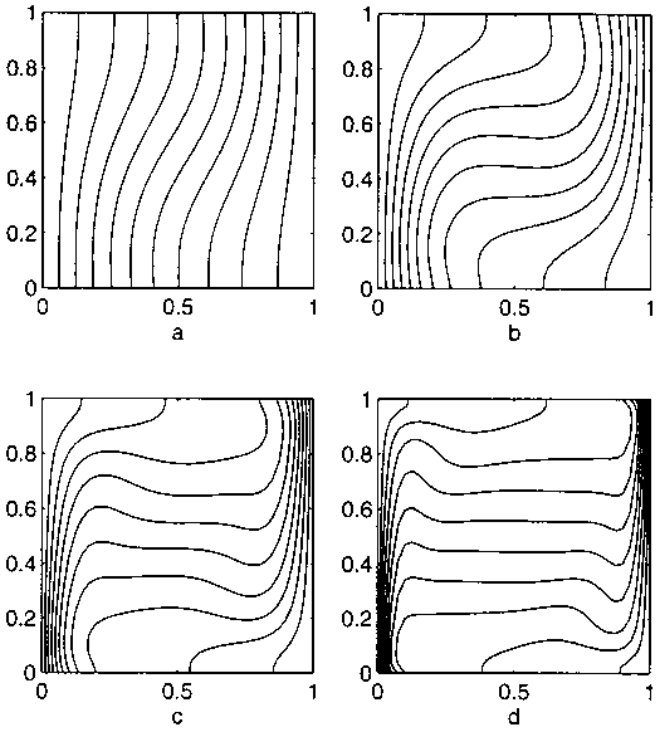

Figure 3. Temperature contours or isotherms for (a) $Ra = 10^3$, (b) $Ra = 10^4$, (c) $Ra = 10^5$, (d) $Ra = 10^6$

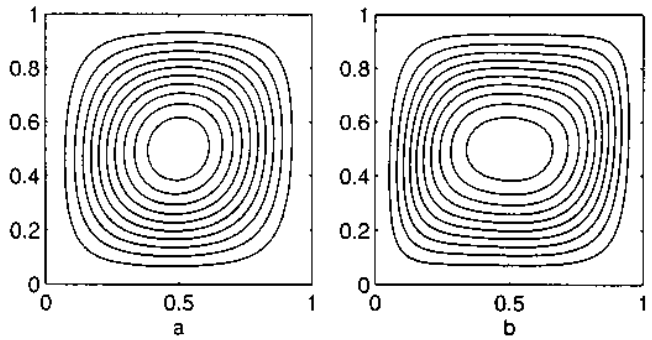

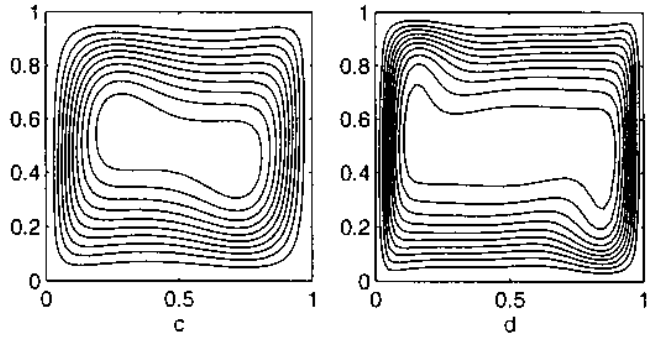

Figure 4.
Streamline pattern for (a) $Ra = 10^3$, (b) $Ra = 10^4$, (c) $Ra = 10^5$, (d) $Ra = 10^6$

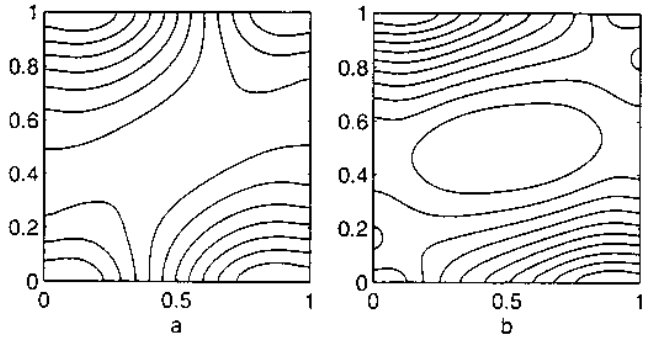

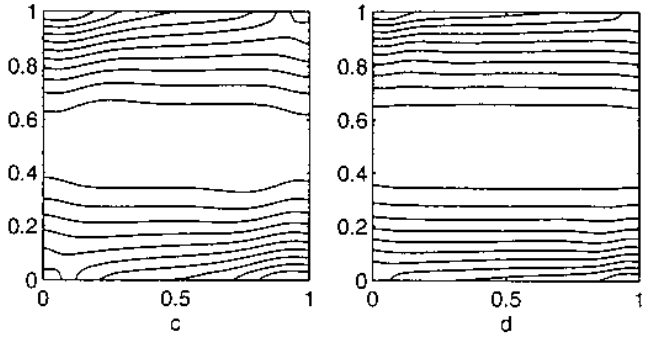

Figure 5.
Pressure contours or isobars for (a) $Ra = 10^3$, (b) $Ra = 10^4$, (c) $Ra = 10^5$, (d) $Ra = 10^6$

The increase in the heat flux due to the increase in the *Ra*, evidenced in the way the isotherms are packed together near the heated walls, can be better observed in the change of the local *Nu* at the hot and cold walls as the *Ra* increases. Figures 6 and 7 show the value of the local *Nu* at the hot right wall and the cold left wall respectively.

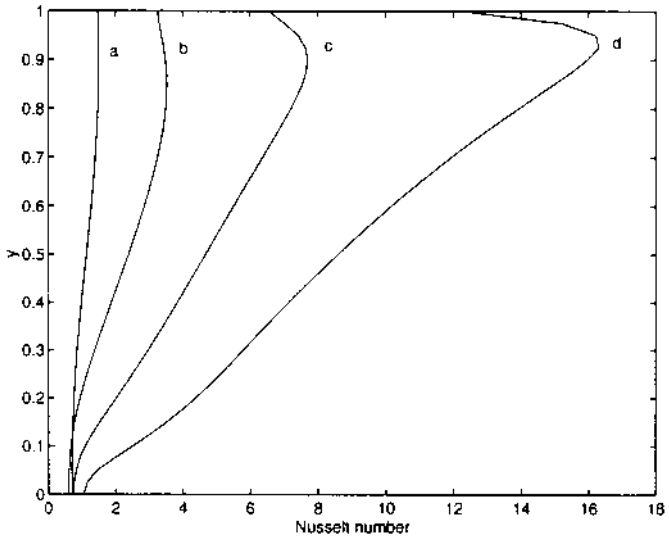

Figure 6.
Hot wall (0, *y*) *Nu* for (a) $Ra = 10^3$, (b) $Ra = 10^4$, (c) $Ra = 10^5$, (d) $Ra = 10^6$

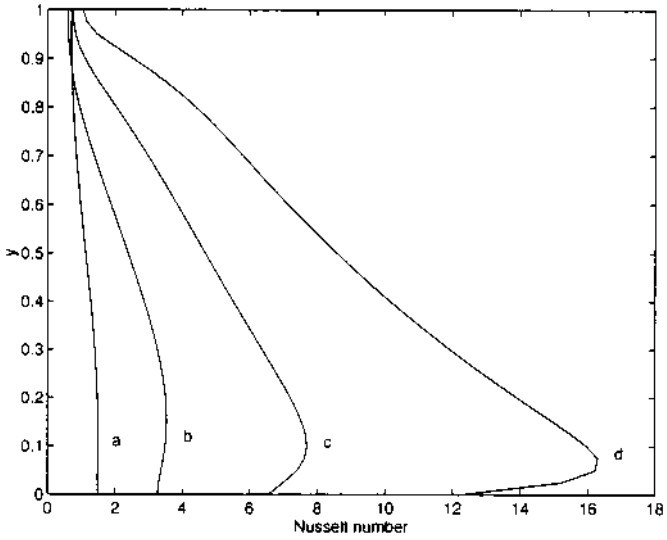

Figure 7.
Cold wall (1, *y*) *Nu* for (a) $Ra = 10^3$, (b) $Ra = 10^4$, (c) $Ra = 10^5$, (d) $Ra = 10^6$

As we can see, the local *Nu* increases as the *Ra*, as expected. We can also observe that the local *Nu* pattern of the cold left wall is the inverted mirror image of the *Nu* pattern of the hot right wall. This is due to our definition of non-dimensional temperature and the choice of its values at the walls. It might be important also to mention that, as can be observed in the plots, the maximum local *Nu* always occurs close to the bottom left-hand corner on the hot right wall, and close to the top left-hand corner on the cold left wall.

Quantitatively, Table I presents and compares our numerical results to those of de Vahl Davis[1]. As expected, the discrepancies between the benchmark solution and the numerical solution hereby presented are within the error margins reported by de Vahl Davis between extrapolated and nodal values of the solutions.

Tables II-V are the results of a grid-dependence study of the benchmark solution for all cases between with *Ra* between 10^3 and 10^6. As can be inferred from the data in these tables, the present numerical solution approaches the benchmark solution as the mesh is refined.

Three-dimensional problem

In the full three-dimensional version of the thermally driven cavity, the flow develops in the *x*, *y* and *z* directions, giving rise to complex fluid flow. Owing to the nature of the problem geometry and its governing equations, we can infer certain aspects of the fluid behaviour in three dimensions.

First of all, the flow is symmetric with respect to the central cross-section at $z = 0.5$, i.e. cross-sections at $z = 0.5 \pm \Delta z$ are identical. This reduces the number

	Ra							
	10^3		10^4		10^5		10^6	
Unknown	M&R	DVD	M&R	DVD	M&R	DVD	M&R	DVD
$\lvert\Psi_{mid}\rvert$	1.193	1.174	5.128	5.071	9.520	9.111	16.366	16.320
$\lvert\Psi_{max}\rvert$	1.193	1.174	5.128	5.071	9.912	9.612	16.754	16.750
x	0.500	0.500	0.500	0.500	0.275	0.285	0.150	0.151
y	0.500	0.500	0.500	0.500	0.575	0.601	0.525	0.547
u_{max}	3.647	3.649	16.300	16.178	34.607	34.730	64.860	64.630
$x = 0.5$, *y*	0.825	0.813	0.817	0.823	0.850	0.855	0.853	0.850
v_{max}	3.713	3.697	19.723	19.617	68.909	68.590	221.276	219.360
x, $y = 0.5$	0.175	0.178	0.117	0.119	0.067	0.066	0.039	0.038
Nu_0	1.117	1.117	2.223	2.238	4.486	4.509	8.800	8.817
Nu_{max}	1.504	1.505	3.490	3.528	7.552	7.717	17.387	17.925
y	0.100	0.092	0.150	0.143	0.083	0.081	0.039	0.038
Nu_{min}	0.694	0.692	0.586	0.586	0.724	0.729	0.975	0.989
y	1.000	1.000	1.000	1.000	1.000	1.000	1.000	1.000

Table I.
Comparison of the numerical results by Moreno and Ramaswamy (M&R) and the benchmark solutions by de Vahl Davis (DVD)

of cross-sections we need to present. Second, for every Ra, the xy cross-section at $z = 0.5$ is almost identical to the two-dimensional solution for the same Ra. This behaviour can be explained by the fact that the two-dimensional driven cavity problem can be interpreted as the solution to the three-dimensional

Unknown	21×21	% error	41×41	% error	DVD
u_{max}	3.638	–0.30	3.647	–0.05	3.649
y	0.800	–1.60	0.825	1.50	0.813
v_{max}	3.691	–0.16	3.713	0.43	3.697
x	0.200	1.10	0.175	–1.60	0.178
Nu_0	1.113	–0.36	1.117	0.00	1.117
Nu_{max}	1.494	–0.73	1.504	–0.07	1.505
y	0.100	8.70	0.100	8.70	0.092
Nu_{min}	0.700	1.16	0.694	0.29	0.692
y	1.000	0.00	1.000	0.00	1.000

Table II. Grid-dependence study of the solution to the two-dimensional benchmark problem for $Pr = 0.71$ and $Ra = 10^3$

Unknown	21×21	% error	41×41	% error	61×61	% error	DVD
u_{max}	16.172	–0.04	16.232	0.33	16.300	0.75	16.178
y	0.800	–2.90	0.825	0.24	0.817	–0.72	0.823
v_{max}	19.543	–0.38	19.689	0.37	19.723	0.54	19.617
x	0.100	–15.9	0.125	5.04	0.117	–1.70	0.119
Nu_0	2.202	–1.61	2.234	–0.18	2.223	–0.67	2.238
Nu_{max}	3.430	–2.78	3.503	–0.71	3.490	–1.08	3.528
y	0.150	4.80	0.150	4.80	0.150	4.80	0.143
Nu_{min}	0.598	2.05	0.588	0.34	0.586	0.00	0.586
y	1.000	0.00	1.000	0.00	1.000	0.00	1.000

Table III. Grid-dependence study of the solution to the two-dimensional benchmark problem for $Pr = 0.71$ and $Ra = 10^4$

Unknown	21×21	% error	41×41	% error	61×61	% error	DVD
u_{max}	34.637	–1.05	34.461	–0.77	34.607	–0.35	34.730
y	0.850	–0.60	0.850	–0.60	0.850	–0.60	0.855
v_{max}	67.221	–2.00	68.464	–0.18	68.909	0.47	68.590
x	0.050	–24.2	0.075	13.63	0.067	1.5	0.066
Nu_0	4.506	–0.07	4.450	–1.31	4.486	–0.51	4.509
Nu_{max}	7.419	–3.86	7.400	–4.11	7.552	–2.14	7.717
y	0.100	23.5	0.075	–7.4	0.083	2.5	0.081
Nu_{min}	0.793	8.78	0.729	0.00	0.724	–0.69	0.729
y	1.000	0.00	1.000	0.0	1.000	0.00	1.000

Table IV. Grid dependence study of the solution to the two-dimensional benchmark problem for $Pr = 0.71$ and $Ra = 10^5$

problem at the central *xy* cross-section when the *z* dimension is infinite. We also expect that, as we get closer to the insulated cavity walls such as the front and back ones, the fluid velocities will decrease in magnitude owing to the no-slip boundary condition. This translates into a reduction of the intensity of convective heat transfer near those cavity walls. In our presentation of the data, isotherm patterns at the cavity walls are not shown.

The heat transfer behaviour of the three-dimensional fluid system as the *Ra* increases is almost identical to that of the two-dimensional one. As the *Ra* increases, the fluid's vertical velocity, *v*, increases in magnitude faster than its *u* and *w* velocities in the regions where the temperature gradient is non-zero, and especially in the regions were the gradient is actually large. This will induce an increase in the local *Nu* at the heated walls as the *Ra* increases. This behaviour is identical to that of the fluid in the two-dimensional simulation.

In terms of the fluid motion, a three-dimensional flow field view would be best but, although available, is not appropriate for enclosed flows, owing to their multi-directional nature. Instead, *xy*, *zy* and *xz* cross-sections are presented for every *Ra* between 10^3 and 10^5.

Table VI presents a series of values obtained from the numerical simulations of the three-dimensional bench mark problem. We will refer to the values in this Table as we discuss the behaviour of the flow.

We begin by examining the numerical results for $Ra = 10^3$. Figure 8 is a collection of temperature contours or isotherm plots of *x* versus *y* cross-sections of the flow, arranged along the *z* axis of the system's volume. As expected, the curvature of the isotherms increases as we move away from the front or back wall. The isotherms at $x = 0.5$ are almost identical to those in Figure 3b, also as expected. Now, if we look closely at the isotherm pattern, the differences in it as we move along the *z* axis are minimal. Moreover, this minimal difference can be attributed to the fact that we are approaching or receding from an insulated wall. Therefore, it follows that if there is any effect due to the newly introduced *w* velocity in the *z* direction, it is almost negligible. This could happen if the *w*

Table V.
Grid-dependence study of the solution to the two-dimensional benchmark problem for $Pr = 0.71$ and $Ra = 10^6$

Unknown	41×41	% error	61×61	% error	DVD
u_{max}	64.240	–0.60	64.860	0.36	64.6300
y	0.859	1.1	0.853	0.35	0.8500
v_{max}	221.461	0.96	221.276	0.87	219.3600
x	0.036	–5.0	0.039	2.9	0.0379
Nu_0	8.800	–0.19	8.800	–0.19	8.8170
Nu_{max}	17.240	–2.82	17.387	–3.00	17.9250
y	0.036	–4.8	0.039	3.2	0.0378
Nu_{min}	0.978	–1.11	0.975	–1.42	0.9890
y	1.000	0.00	1.000	0.00	1.0000

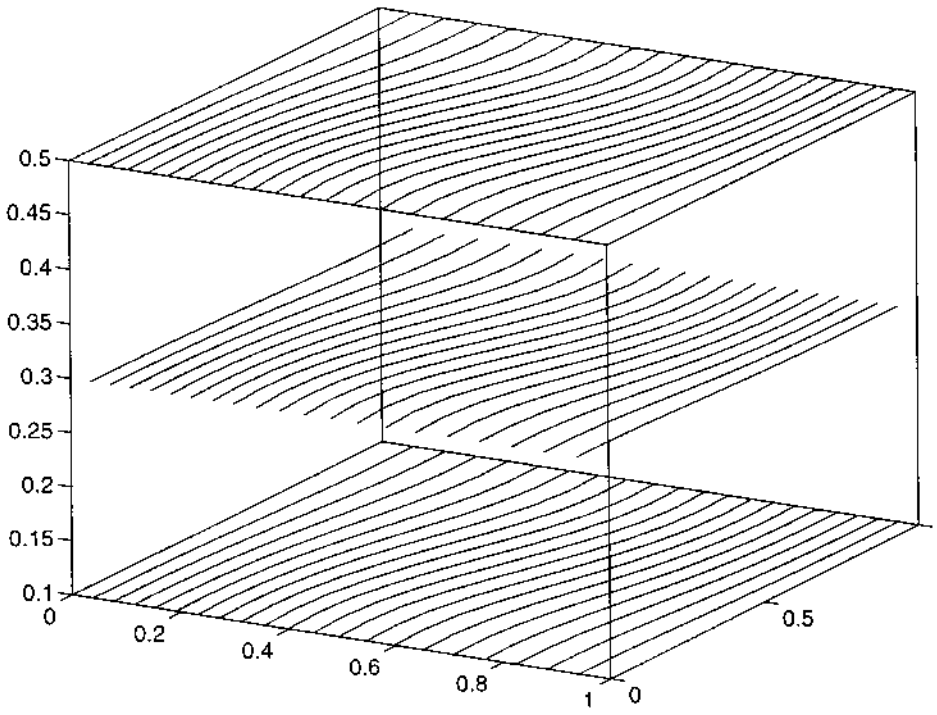

Figure 8. Temperature contour plots at three different cross-sections ($x = 0.1$, $x = 0.3$ and $x = 0.5$) for the fully three-dimensional flow inside a cubic cavity for $Ra = 10^3$

velocity is really small in comparison to the u and v velocities. It turns out that this is exactly the case.

Figures 9-11 present velocity vector field plots at different cross-sections in the three major axes, z, x and y respectively. As we can observe in Table VI the u and v velocities are much larger than the w velocity, as we inferred from the

	Ra			
Unknown	10^3	10^4	10^5	10^6
u_{max}	3.1265	16.6227	39.3957	106.2115
v_{max}	3.8458	19.1779	71.3212	210.3447
w_{max}	0.4226	1.4960	7.2089	23.9156
Nu_0	1.0605	2.1378	4.6722	8.3862
Nu_{max}	1.3559	3.5730	7.4681	17.6733
y	0.1	0.125	0.125	0.05
z	0.5	0.4	0.4	0.75
Nu_{min}	0.7788	0.6122	0.8856	1.0427
y	1.0	1.0	1.0	1.0
z	0.5	0.6	0.4	0.125

Table VI. Important numerical results for the three-dimensional benchmark problem simulation

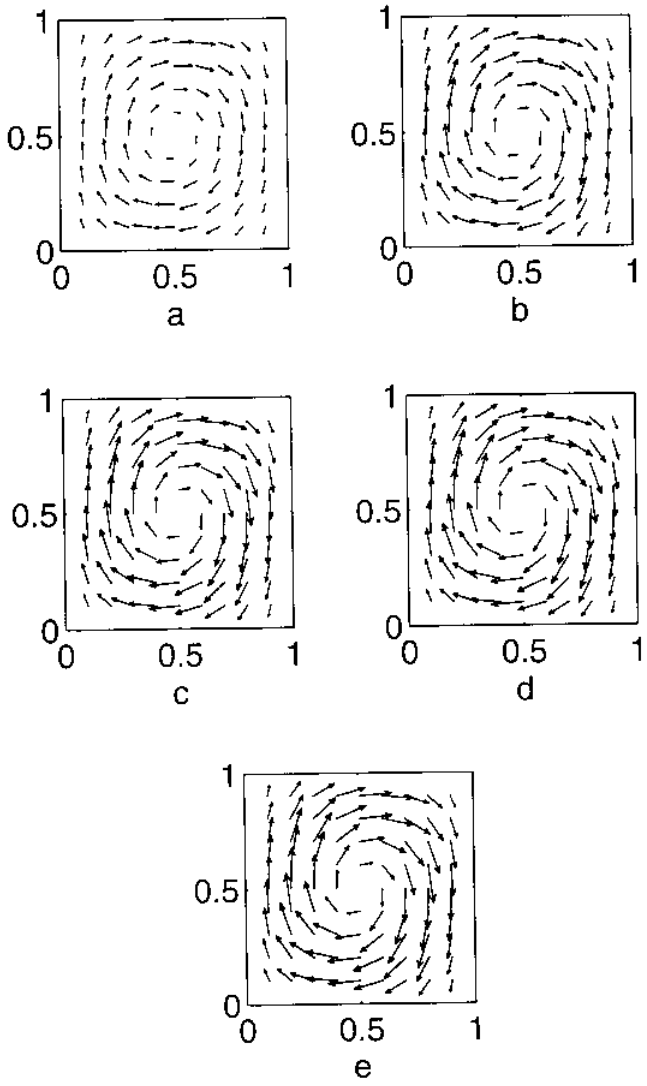

Figure 9.
Vector plots for y versus x cross-sections at (a) $z = 0.1$, (b) $z = 0.2$, (c) $z = 0.3$, (d) $z = 0.4$, (e) $z = 0.5$ for $Ra = 10^3$

isotherm patterns. The w velocity is both seven times smaller than the u velocity, and about nine times smaller than the v velocity. That is why the temperature contour plots do not change in shape much as we move along the z axis. We also observe that the effect of w is minimal when we examine the available vector field plots. Figure 10 is a collection of y versus z cross-sections of the flow along the x axis. Therefore the arrows represent the resultants of the v velocity vector in the y direction and the w velocity vector in the z direction. Nevertheless, the resultants are mostly parallel to the z axis. In Figure 11 we have z versus x cross-sections of the flow along the y axis, such that the arrows

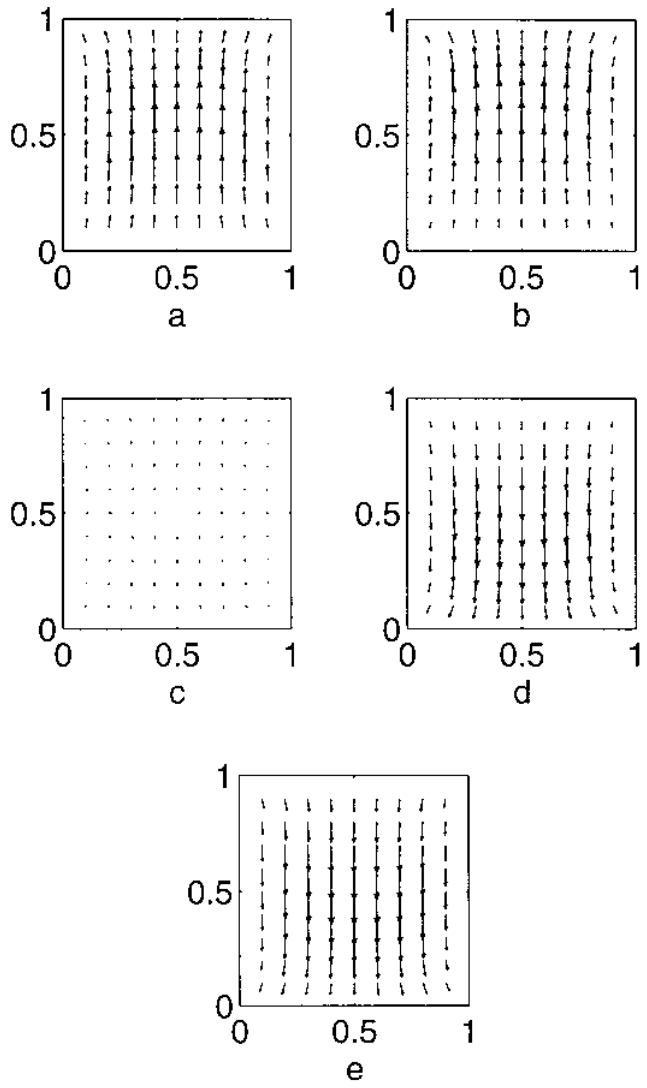

Figure 10.
Vector plots for y versus z cross-sections at (a) $x = 0.1$, (b) $x = 0.3$, (c) $x = 0.5$, (d) $x = 0.7$, (e) $x = 0.9$ for $Ra = 10^3$

represent the resultants of the vector sum of the w vector in the z direction and the u velocity in the x direction. Notice that the resultants are mostly parallel to the x axis. Therefore, we conclude without a doubt that the effect of w in the flow is negligible for $Ra = 10^3$. Moreover, Figures 10c and 11c show that when the v and u velocities are small, the resultant vectors are almost zero, in other words, w is negligible. So, the flow rotates clockwise almost uniformly around the z axis without any significant change as we move in the z direction.

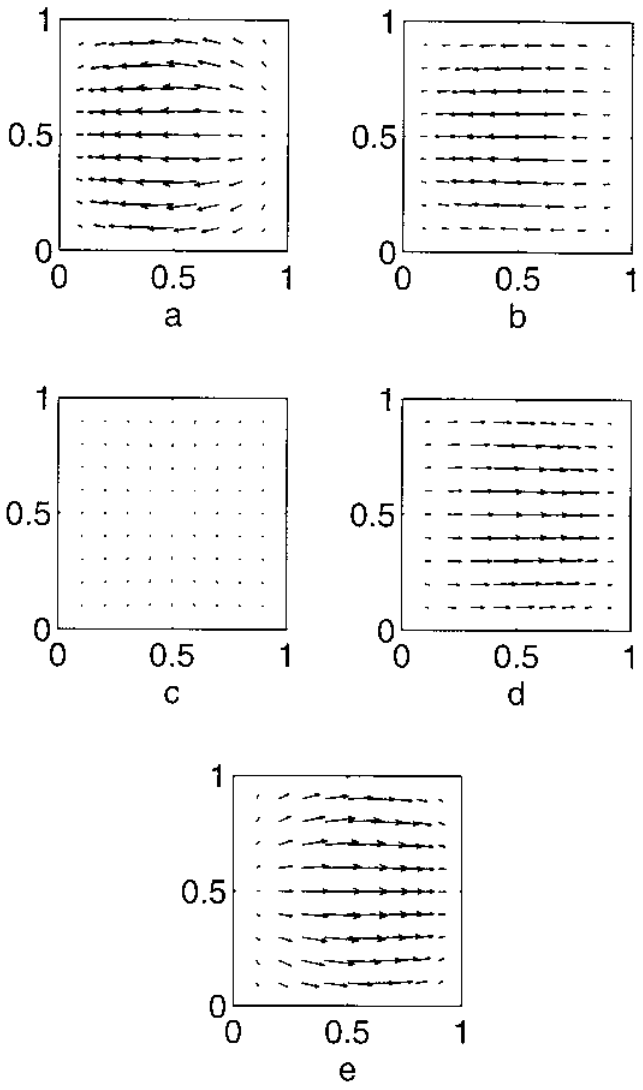

Figure 11.
Vector plots for z versus x cross-sections at (a) $y = 0.1$, (b) $y = 0.3$, (c) $y = 0.5$, (d) $y = 0.7$, (e) $y = 0.9$ for $Ra = 10^3$

Figures 12 and 13 show the local Nu surface over the hot left wall and the cold right wall of the cavity, respectively. We can see that the distribution of the local Nu is very similar to that of the two-dimensional benchmark. The Nu at the hot wall is at its maximum close to its bottom, and minimum at its top. Inversely, the local Nu at the cold wall is maximum near its top portion, and minimum at the bottom. In fact, as one can see in Table VI the maximum value of the local Nu is almost identical to that of the two-dimensional solution. It also occurs at the $z = 0.5$ cross-section, as predicted from the geometric configuration.

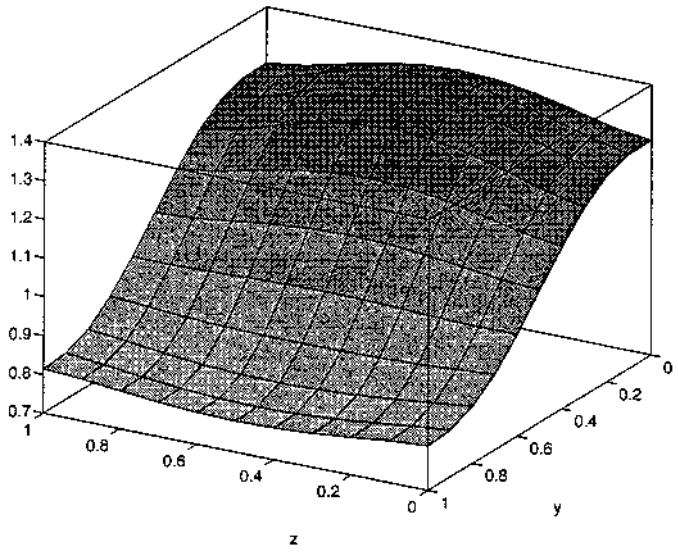

Figure 12.
Hot wall (0, *y*, *z*) *Nu* for $Ra = 10^3$

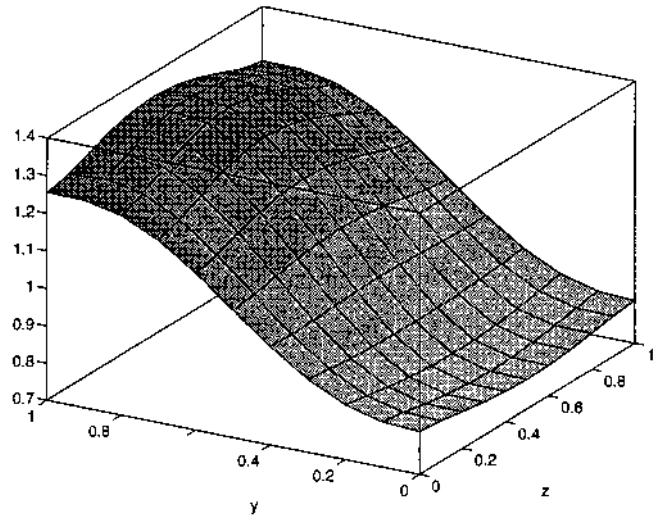

Figure 13.
Hot wall (0, *y*, *z*) *Nu* for $Ra = 10^3$

For $Ra = 10^4$, the flow's behaviour is very similar to that at 10^3. Figure 14 is also a collection of temperature contours of *x* versus *y* cross-sections along the *z* axis. Again we observe an increase in isotherm curvature as we move away from the insulated front wall along the *z* axis. Nevertheless, the curvature increase is too low to be a result of *w* velocity influence. So, we conclude as before that the *w* velocity must be much smaller in magnitude than either the *u* or *v* velocities. The vector plots in Figures 15-17 support that conclusion. Resultant vectors

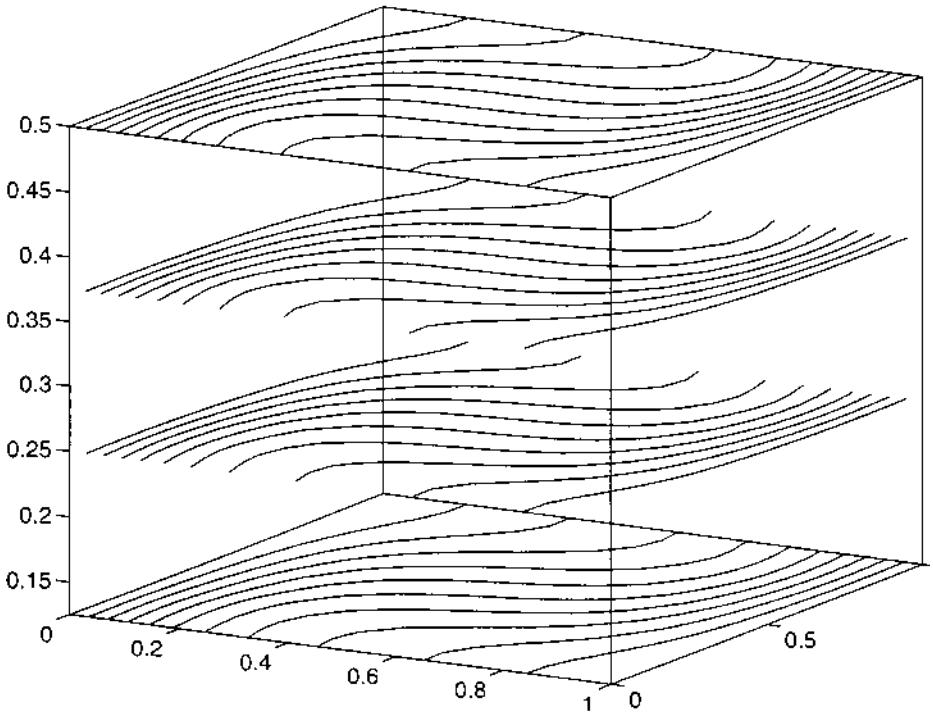

Figure 14.
Temperature contour plots at four different cross-sections ($x = 0.125$, $x = 0.25$, $x = 0.375$ and $x = 0.5$) for the fully three-dimensional flor inside a cubic cavity for $Ra = 10^4$

parallel to the y axis in plots of y versus z cross-sections indicate v velocities much larger than w. In the same fashion, resultant vectors parallel to the x axis in z versus x cross-section plots indicate u velocities much larger than w velocities. Vector plots in which the resultants are almost zero support the conclusion that the w velocity has a minimal effect on the fluid flow. As inferred from the graphic information, Table VI shows that the w velocity is in fact both 11 times smaller than the w velocity, and about 13 times smaller than the v velocity. Therefore, owing to the negligible effect of w on the flow, the fluid rolls clockwise about the z axis, very much like it does when the $Ra = 10^3$. At $Ra = 10^4$, however, the circulation cell elongates in the x direction such that the central region of stationary and slowly moving fluid becomes almost twice as wide as that observed at a $Ra = 10^3$.

The local Nu surfaces for both the hot and cold walls can be seen in Figures 18 and 19, respectively. The average value of the local Nu and its maximum value, together with its location, can be found in Table VI. Notice that these values are very close to those of the two-dimensional problem at the same Ra.

For $Ra = 10^5$, the flow exhibits certain significant changes when compared with previous cases with different Ra. Figure 20 is again a collection of temperature contours of x versus y cross-sections along the z axis.

The already observed increase in isotherm curvature as we move away from the insulated front wall along the z axis is now more pronounced. In contrast

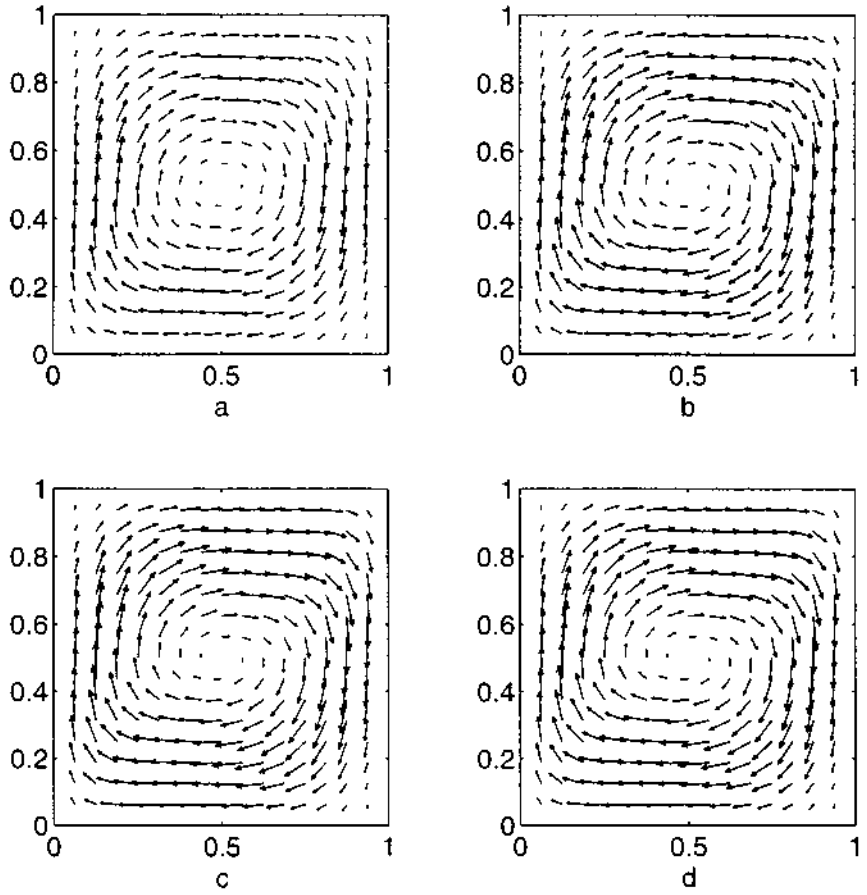

Figure 15.
Vector plots for y versus x cross-sections at (a) $z = 0.125$, (b) $z = 0.25$, (c) $z = 0.375$ and (d) $z = 0.5$ for $Ra = 10^4$

with cases with lower Ra, the curvature increase is too high to be explained solely by the closeness of the insulated walls, so we must conclude that it must be influenced by the w velocity. We also conclude that the w velocity must have increased with the Ra, although, as before, it must be much smaller in magnitude than either the u or v velocities. This is because although the curvature has changed prominently, the overall isotherm pattern has not changed qualitatively. The vector plots in Figures 21-23 support that conclusion. Resultant vectors parallel to the y axis in plots of y versus z cross-sections indicate v velocities much larger than w. Nevertheless, when compared to similar plots for lower Ra the effect of w on the fluid motion is more visible now, specially in the bottom near the insulated front wall, and at the top near the insulated back wall. Similarly, resultant vectors parallel to the x axis in z versus x cross-section plots indicate u velocities much larger than w velocities. Table VI indicates that the w velocity is five times smaller than the u velocity, and at the same time ten times smaller than the v velocity. This is a considerable

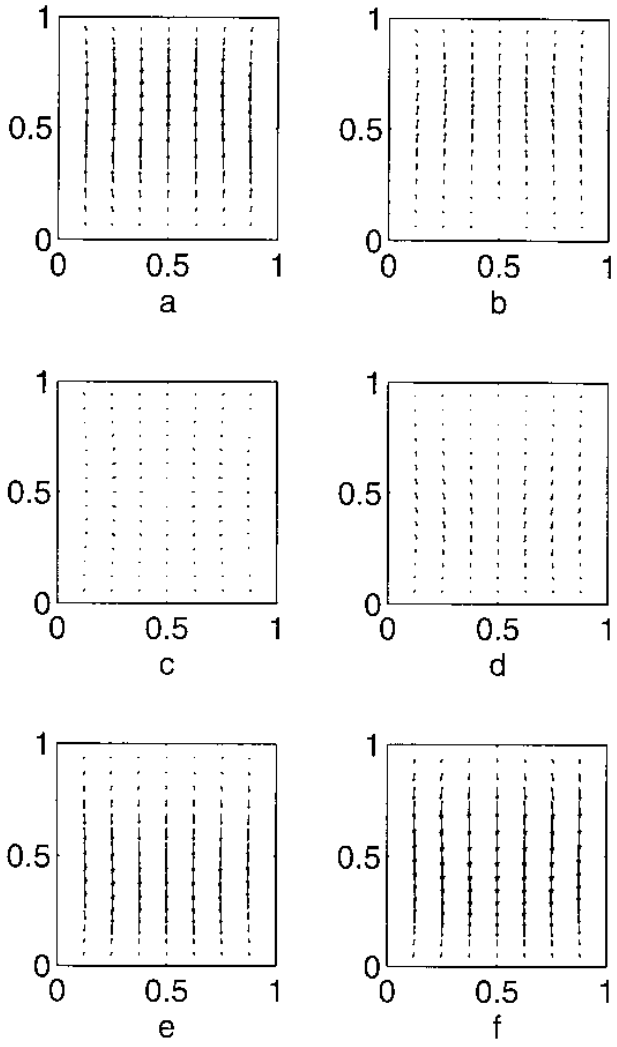

Figure 16.
Vector plots for y versus z cross-sections at (a) $x = 0.1875$, (b) $x = 0.3125$, (c) $x = 0.5$, (d) $x = 0.625$, (e) $x = 0.75$, (f) $x = 0.875$ for $Ra = 10^4$

increase in the relative magnitude of w, if we compare it with that at lower Ra. The local Nu pattern reflects the effect of the w velocity on the fluid's behaviour. For lower Ra the change in the local Nu in the z direction is very smooth and gradual. However, for $Ra = 10^5$, the local Nu changes rapidly in the z direction to a maximum, specially in the regions where the w velocity seems to have a comparable effect with that of the v and u velocities, as can be seen in Figures 24 and 25. Table VI provides values and locations for the maximum and minimum local Nu.

Although the w velocity starts to play an important role on the fluid's behaviour, the overall flow movement is very much like that at $Ra = 10^3$ and $Ra = 10^4$. The fluid rolls clockwise around the z axis. However, the circulation cell

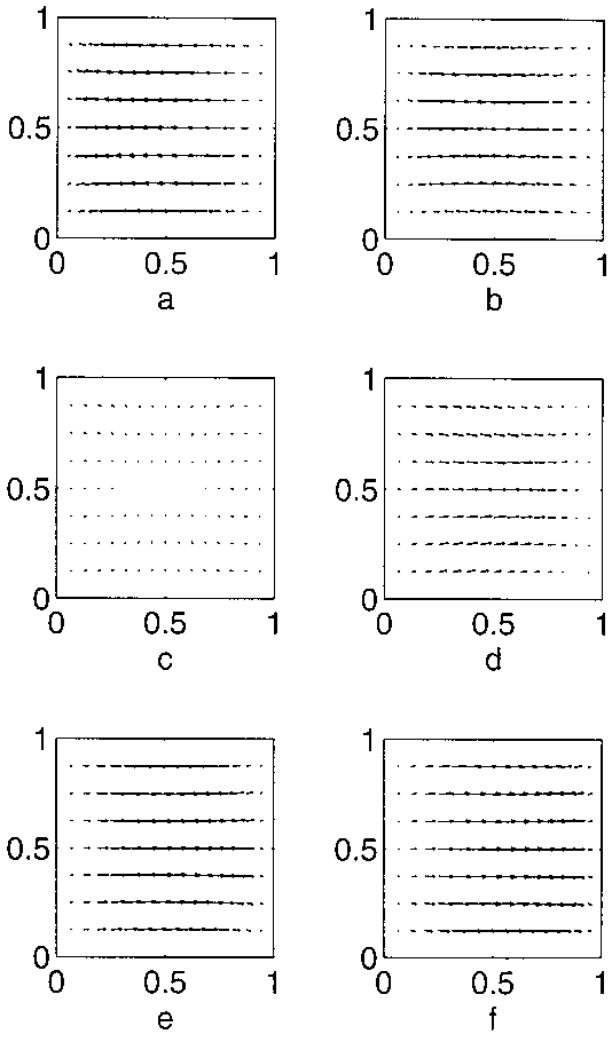

Figure 17. Vector plots for z versus x cross-sections at (a) $y = 0.1875$, (b) $y = 0.3125$, (c) $y = 0.5$, (d) $y = 0.625$, (e) $y = 0.75$, (f) $y = 0.875$ for $Ra = 10^4$

present in previous cases finally changes shape into two interconnected cells which are inverted mirror images of each other.

For $Ra = 10^6$, the convective effects simply dominate the flow pattern. The two circulation cells observed at $Ra = 10^5$ gain strength and elongate in the y direction. The effects on the temperature distribution can be observed in the temperature contours of x versus y cross-sections along the z axis in Figure 26.

The pronounced increase in isotherm curvature is a direct result of the dominant role of convection at this Ra number. The vector plots in Figures 27-29 support that conclusion. Resultant vectors parallel to the y axis in plots of y versus z cross-sections indicate v velocities much larger than w. Nevertheless, when compared to similar plots for lower Ra the effect of w on the fluid motion

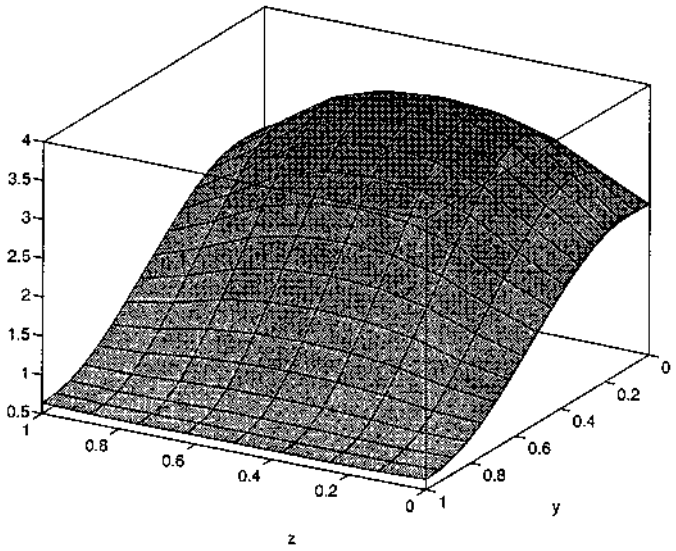

Figure 18.
Hot wall (0, *y*, *z*) *Nu* for $Ra = 10^4$

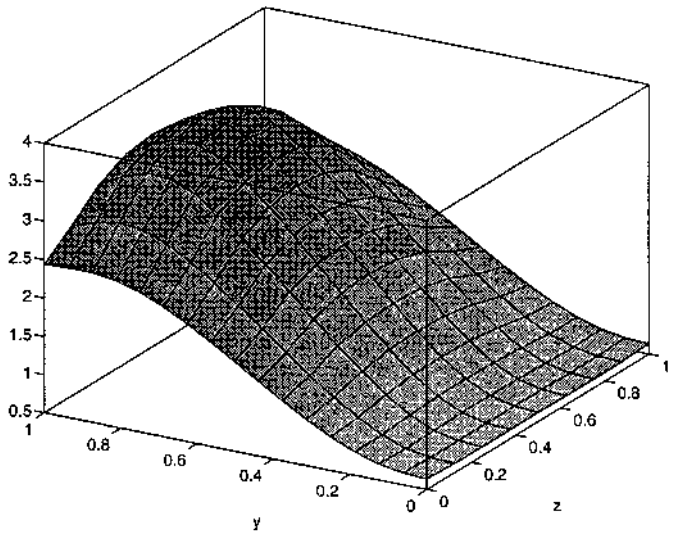

Figure 19.
Cold wall (0, *y*, *z*) *Nu* for $Ra = 10^4$

is more visible now, specially in the bottom near the insulated front wall, and at the top near the insulated back wall. Similarly, resultant vectors parallel to the *x* axis in *z* versus *x* cross-section plots indicate *u* velocities much larger than *w* velocities. However, Table VI indicates that the *w* velocity is five times smaller than the *u* velocity, and at the same time nine times smaller than the *v* velocity, a considerable increase in the relative magnitude of *w*. The local *Nu* pattern changes rapidly in the *z* direction to a maximum in the regions where the *w* velocity seems to have a more pronounced effect as can be seen in Figures 30

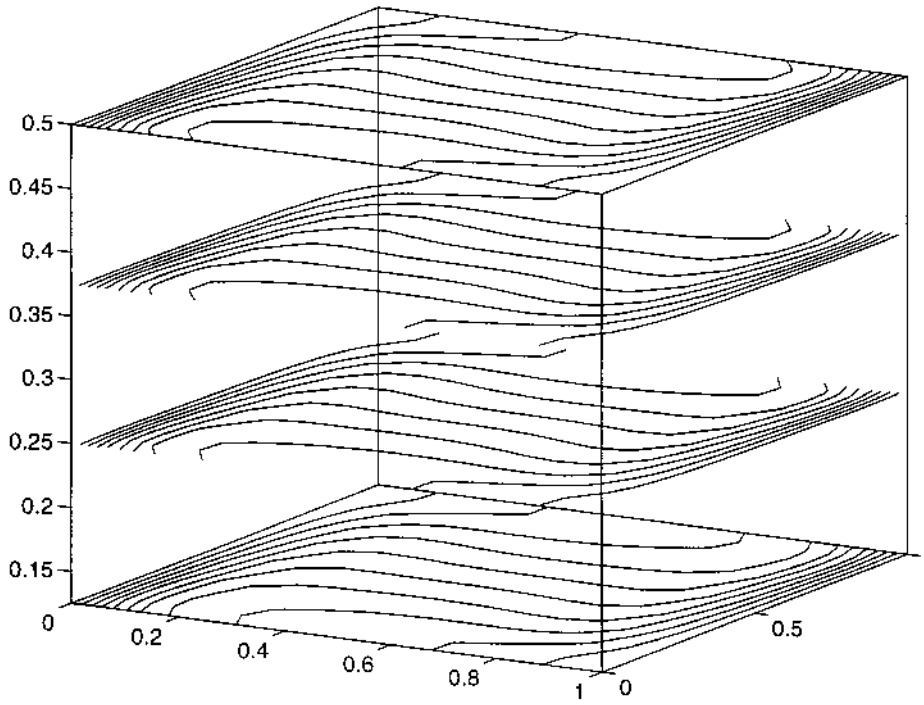

Figure 20. Temperature contour plots at four different cross-sections ($x = 0.125$, $x = 0.25$, $x = 0.375$ and $x = 0.5$) for the fully three-dimensional flow inside a cubic cavity for $Ra = 10^5$

and 31. Table VI provides values and locations for the maximum and minimum local *Nu*.

Our results can be qualitatively compared to those of Pepper[8]. In his work, the thermally-driven cavity problem with its primitive variable equations is solved by using a time-split finite element scheme similar to the Petrov-Galerkin formulation. There are no quantitative results in his paper, nevertheless, his qualitative results and ours are in agreement.

On the other hand, the work by Fusegi *et al.*[9] quantifies many of the flow characteristics in three dimensions and compares them with those of de Vahl Davis[1] in two dimensions.

Table VII shows a comparison between our numerical simulations and those by Fusegi *et al.* In their particular study, an irregular grid of $62 \times 62 \times 62$ grid points was used to resolve the flow field, in contrast with our $41 \times 41 \times 17$ grid points regular mesh. It is evident in the comparison that the differences in locations of the relevant characteristic numbers of the flow are in general within the difference in resolution of our meshes. More important is the fact that, even without taking these mesh differences into account, the mean percentage error between the results is about 4 per cent.

Figures 32 and 33 are isosurface plots of the temperature and the u, v and w velocity fields for $Ra = 10^4$ and $Ra = 10^6$, respectively. Although we cannot

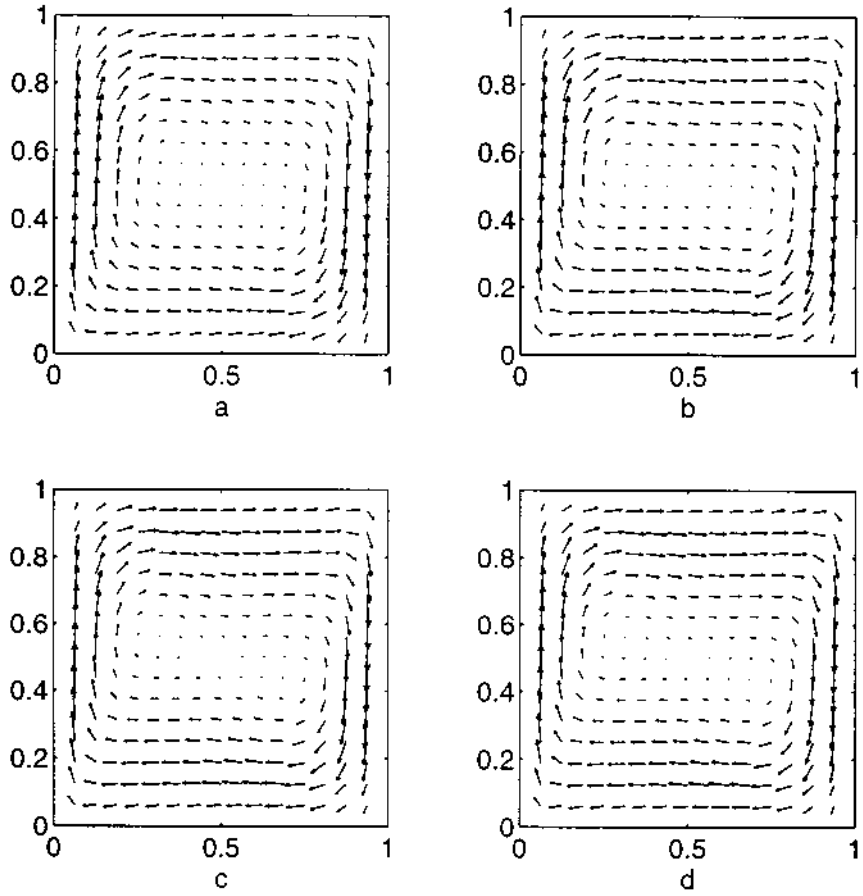

Figure 21.
Vector plots for y versus x cross-sections at (a) $z = 0.125$, (b) $z = 0.25$, (c) $z = 0.375$, (d) $z = 0.5$ for $Ra = 10^5$

	Ra							
	10^3		10^4		10^5		10^6	
Unknown	M&R	FEA	M&R	FEA	M&R	FEA	M&R	FEA
u_{max}	0.1321	0.1314	0.1983	0.2013	0.1587	0.1468	0.1320	0.08416
y	0.1750	0.2000	0.1750	0.1833	0.1250	0.1453	0.0500	0.1443
v_{max}	0.1337	0.1320	0.2210	0.2252	0.2412	0.2471	0.2416	0.2588
x	0.8250	0.8333	0.8750	0.8833	0.9250	0.9353	0.9750	0.9669
Nu_{max}	1.4191	1.4200	3.6104	3.6520	7.8709	7.7950	16.5170	17.6700
y	0.1000	0.0833	0.1500	0.6232	0.1000	0.08256	0.0500	0.03793
Nu_{min}	0.7306	0.7639	0.5624	0.6110	0.7139	0.7867	1.0874	1.2570
y	1.0000	1.0000	1.0000	1.000	1.0000	1.0000	1.0000	1.0000
Nu_{mean}	1.0875	1.1050	2.2363	2.3020	4.5776	4.6460	8.8168	9.012

Table VII.
Comparison of the numerical results by Moreno and Ramaswamy (M&R) and the solutions by Fusegi *et al.* (FEA)

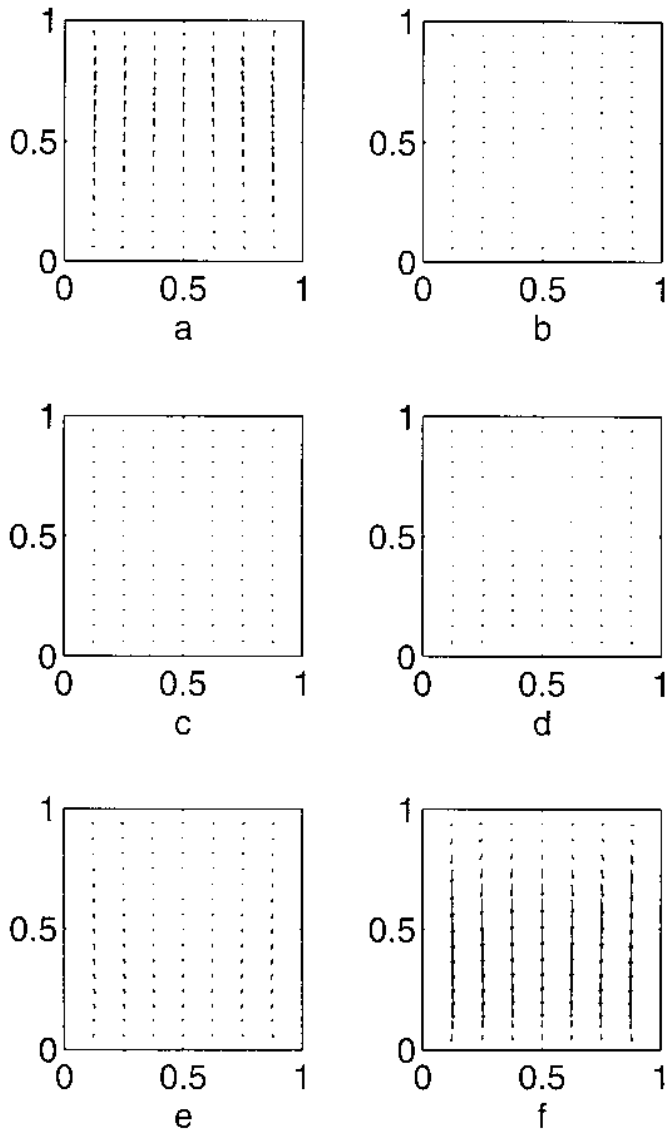

Figure 22. Vector plots for y versus z cross-sections at (a) $x = 0.1875$, (b) $x = 0.3125$, (c) $x = 0.5$, (d) $x = 0.625$, (e) $x = 0.75$, (f) $x = 0.875$ for $Ra = 10^5$

resolve all the contour levels that Fusegi *et al.*[9] present, the levels that are present in both results are in excellent agreement.

In particular, these plots help visualize how the inner core of the fluid in the cavity becomes near stagnant, as well as how the temperature stratifies in the same region as the Rayleigh number increases. It is clear that any three-dimensional effects as depicted by the w-velocity component migrate from the centre of the cavity and become only prominent near the cavity's corners. It is also of interest to observe how the u and v velocity components are confined to

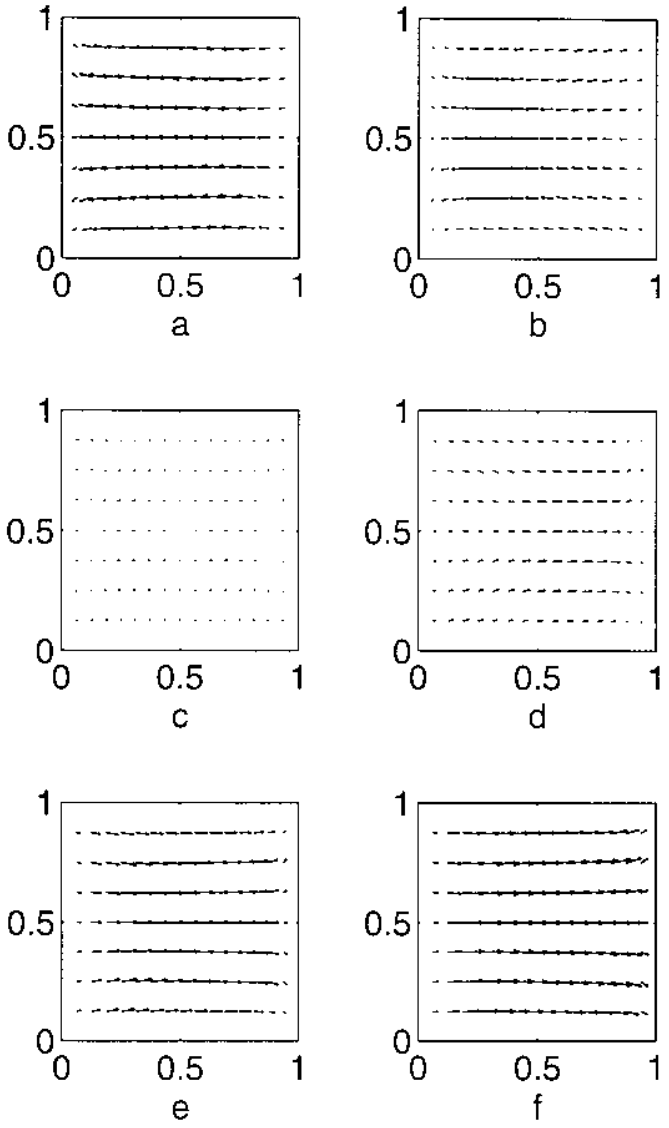

Figure 23.
Vector plots for z versus x cross-sections at (a) $y = 0.1875$, (b) $y = 0.3125$, (c) $y = 0.5$, (d) $y = 0.625$, (e) $y = 0.75$, (f) $y = 0.875$ for $Ra = 10^5$

the regions closest to the isothermal walls and the top and bottom walls of the cavity as the Rayleigh number increases.

Concluding remarks

An iterative finite difference analysis is performed to study the feasibility of using such a scheme for the simulation of two- and three-dimensional thermally driven flows. The first part of this investigation involves deriving the finite difference formulas required in the application of the fractional step method for

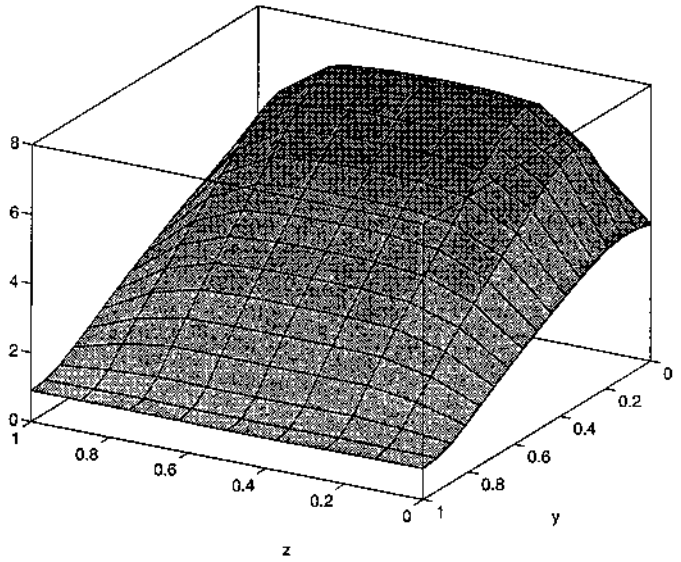

Figure 24.
Hot wall (0, *y*, *z*) *Nu* for $Ra = 10^5$

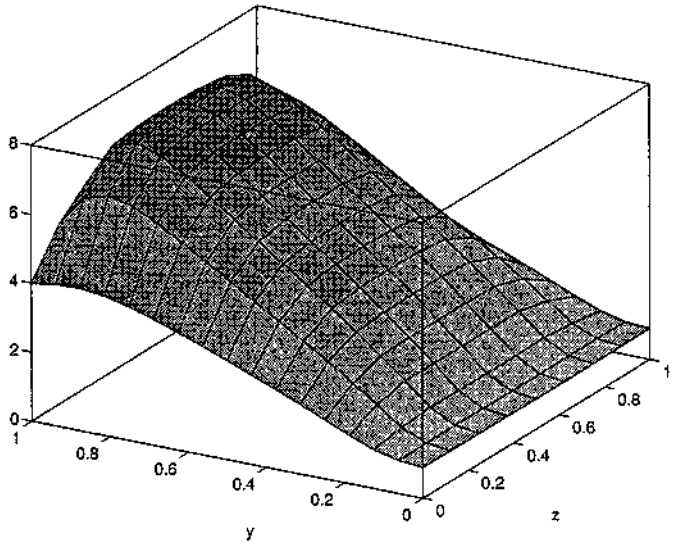

Figure 25.
Cold wall (0, *y*, *z*) *Nu* for $Ra = 10^5$

the solution of the Navier-Stokes and energy equations, as well as implementing the point successive over-relaxation (PSOR) for the solution of the resulting system of equations. The second part intends to validate the solution scheme by solving the well-known benchmark problem of the thermally driven square cavity. The results obtained agree well with benchmark results for low and high Rayleigh numbers. In addition, we extend the two-dimensional problem into three dimensions by solving the problem of a thermally-driven cubic cavity. Steady state solutions of this problem when the walls in the third dimension are

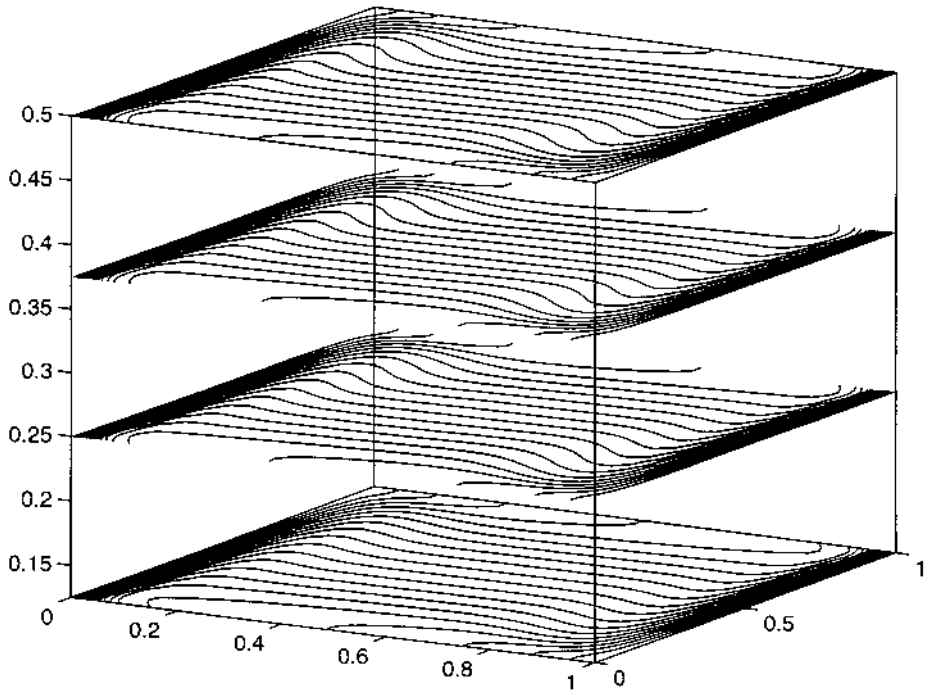

Figure 26.
Temperature contour plots at four different cross-sections ($x = 0.125$, $x = 0.25$, $x = 0.375$ and $x = 0.5$) for the fully three-dimensional flow inside a cubic cavity for $Ra = 10^6$

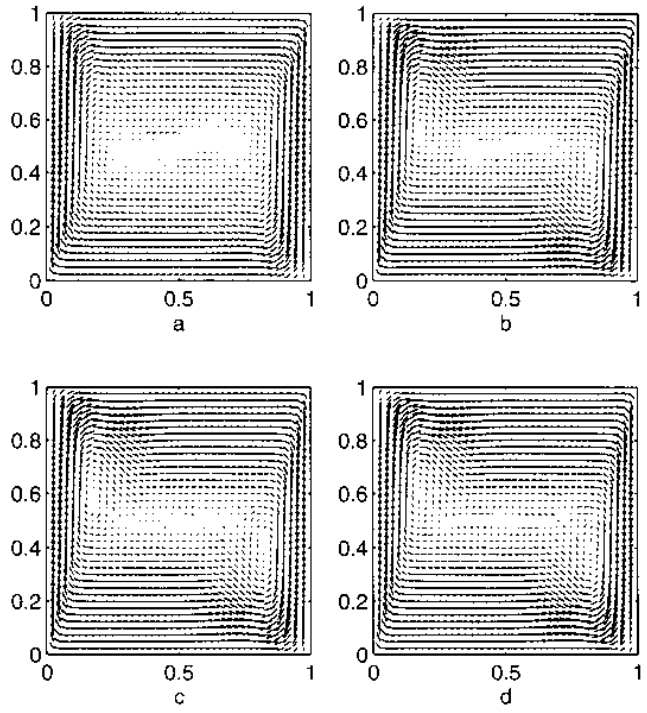

Figure 27.
Vector plots for y versus x cross-sections at (a) $z = 0.125$, (b) $z = 0.25$, (c) $z = 0.375$, (d) $z = 0.5$ for $Ra = 10^6$

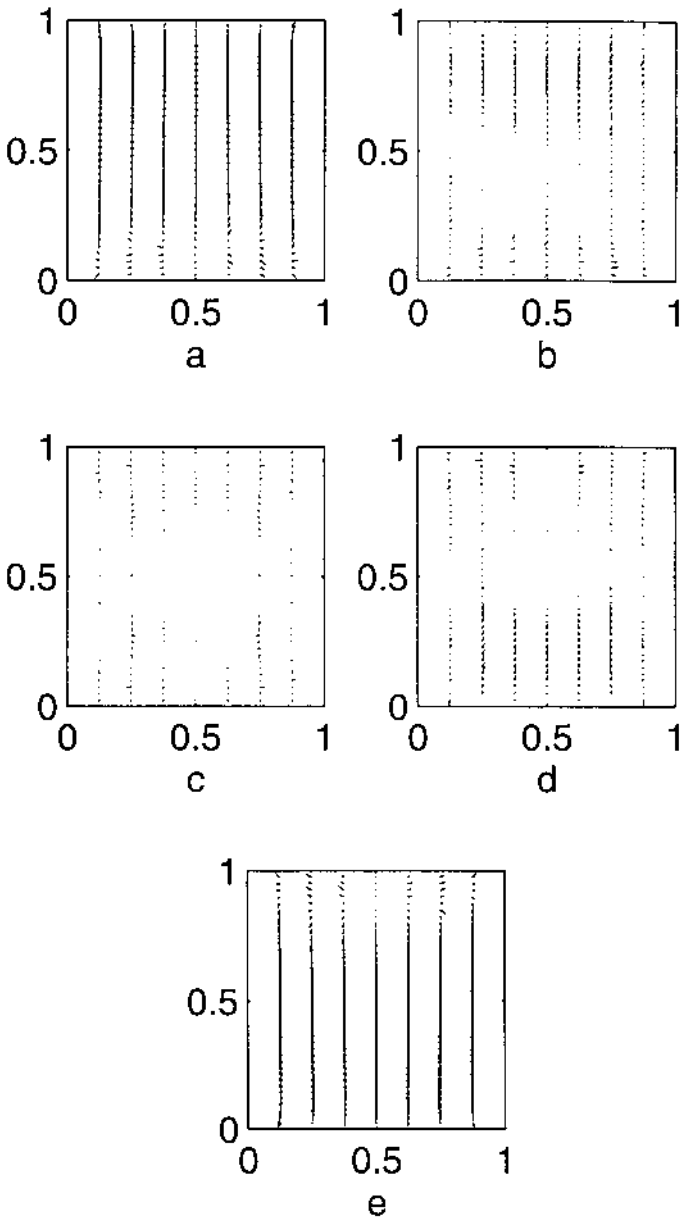

Figure 28.
Vector plots for y versus z cross-sections at (a) $x = 0.1$, (b) $x = 0.3$, (c) $x = 0.5$, (d) $x = 0.7$, (e) $x = 0.9$ for $Ra = 10^6$

kept insulated indicate little effect of the third velocity component on the flow pattern other than that due to the no slip boundary condition. In general, for this conditions, the fluid rolls around the third dimension without major changes, as if the two-dimensional solution has been projected along the new axis. Our results agree well with other three-dimensional extensions of the

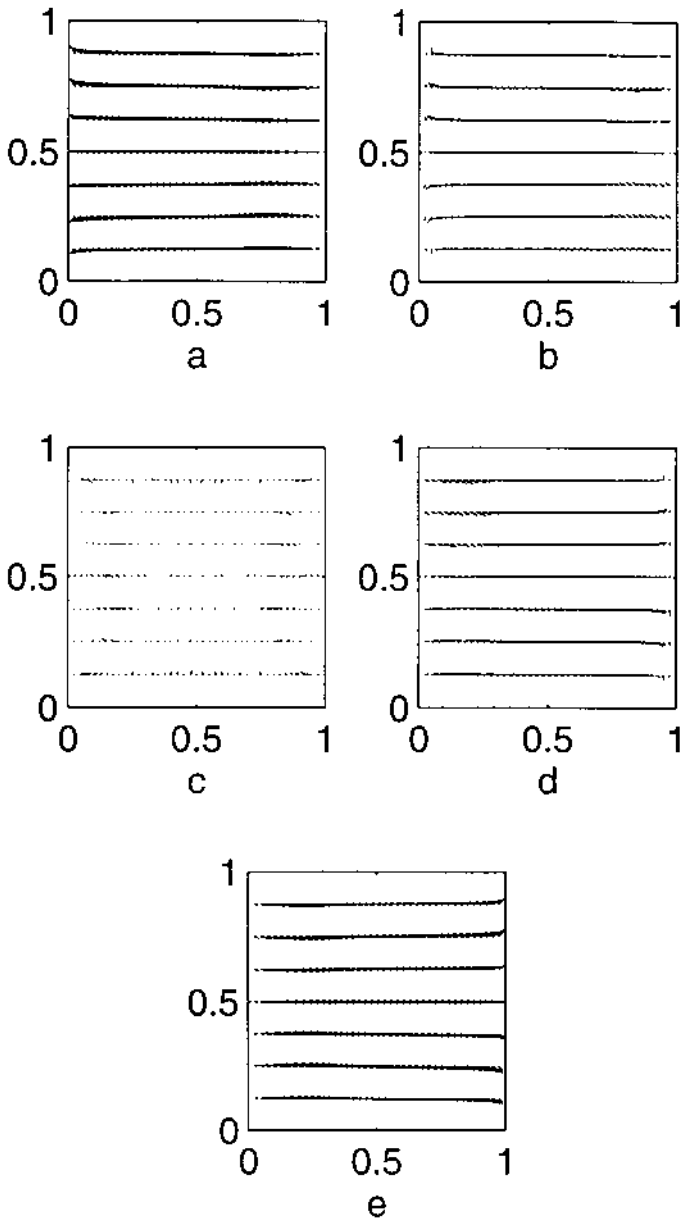

Figure 29.
Vector plots for z versus x cross-sections at (a) $x = 0.1$, (b) $x = 0.3$, (c) $x = 0.5$, (d) $x = 0.7$, (e) $x = 0.9$ for $Ra = 10^6$

benchmark problem available in the literature. Thanks to this benchmark study we conclude that the solution method is accurate, that it allows the user easily to control aspects of the solution process such as required CPU time and accuracy, and that it is capable of simulating both two- and three-dimensional problems within acceptable time limits.

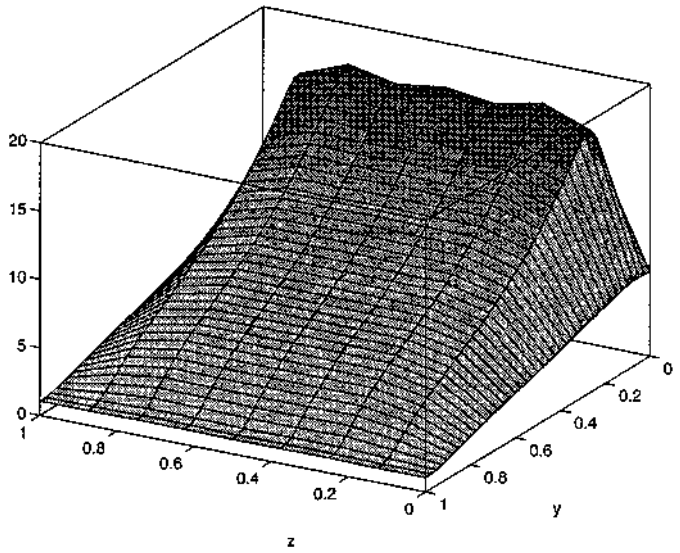

Figure 30.
Hot wall (0, *y*, *z*) *Nu* for $Ra = 10^6$

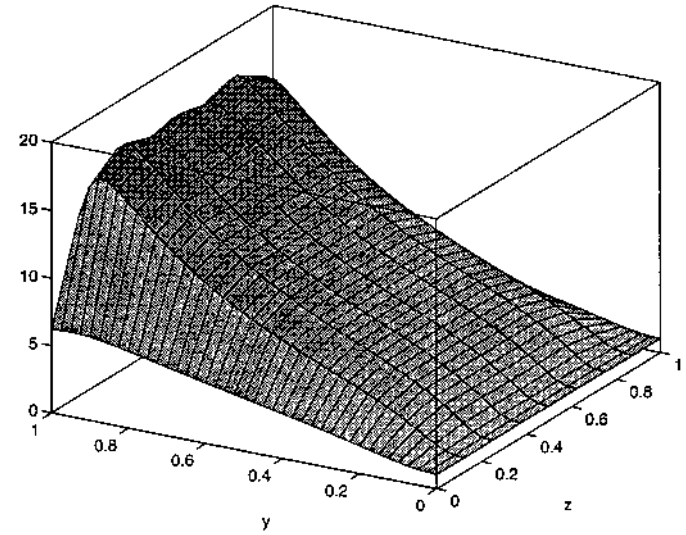

Figure 31.
Cold wall (0, *y*, *z*) *Nu* for $Ra = 10^6$

After validating the present scheme, it is only natural to attack a number of more complex problems. Part II of this series presents results for two- and three-dimensional simulations of enclosed natural convective flows in complex geometries.

In these geometries, internal bodies as well as variations in aspect ratio across the domain of interest partition it in such a manner that different regions of the cavities in question experience boundary conditions similar to those seen in several classical problems in natural convection. In that way, we can study

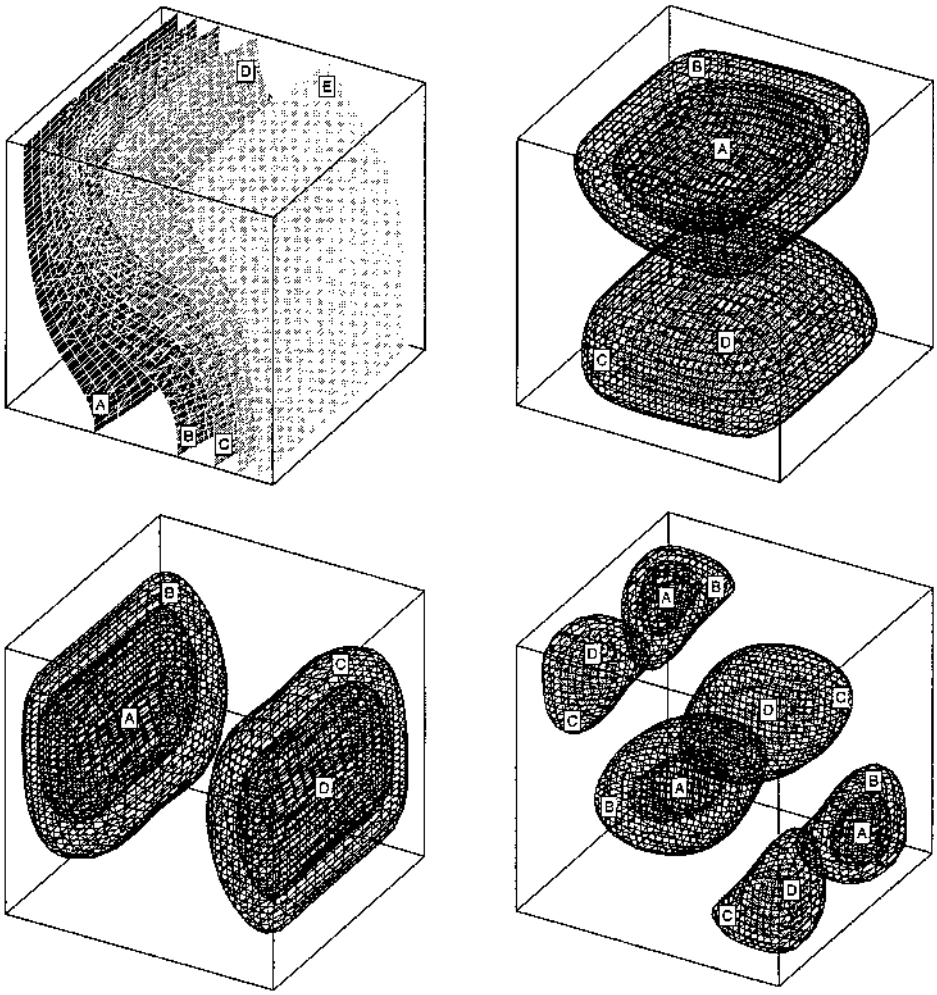

Figure 32.
Top left: temperature contours inside the cavity for $Ra = 10^4$. Contour levels: (A) 0.9667, (B) 0.9833, (C) 1.0, (D) 1.017, (E) 1.033. Top right to bottom right: isovelocity contours for *u*-velocity, *v*-velocity and *w*-velocity components respectively for $Ra = 10^4$. Contour levels for *u*: (A) –0.1333, (B) –0.06667, (C) 0.06667, (D) 0.1333. Contour levels for *v*: (A) –0.15, (B) –0.075, (C) 0.075, (D) 0.15. Contour levels for *w*: (A) –0.01667, (B) –0.008333, (C) 0.008333, (D) 0.01667

the interactions of such classic flows as buoyancy effects which become more and more dominant. We will show how such interactions produce strong three-dimensional effects that lead to unexpected fluid motions and heat transfer enhancements and detriments all over these particular domains.

References

1. de Vahl Davis, G., "Natural convection of air in a square cavity: a bench mark numerical solution", *International Journal for Numerical Methods in Fluids*, Vol. 3, 1983, pp. 249-64.
2. Saitoh, T. and Hirose, K., "High-accuracy bench mark solutions to natural convection in a square cavity", *Computational Mechanics*, Vol. 4, 1989, pp. 17-27.
3. Anderson, D.A., Tannehill, J.C. and Pletcher, R.H., *Computational Fluid Mechanics and Heat Transfer*, McGraw-Hill, New York, NY, 1984.

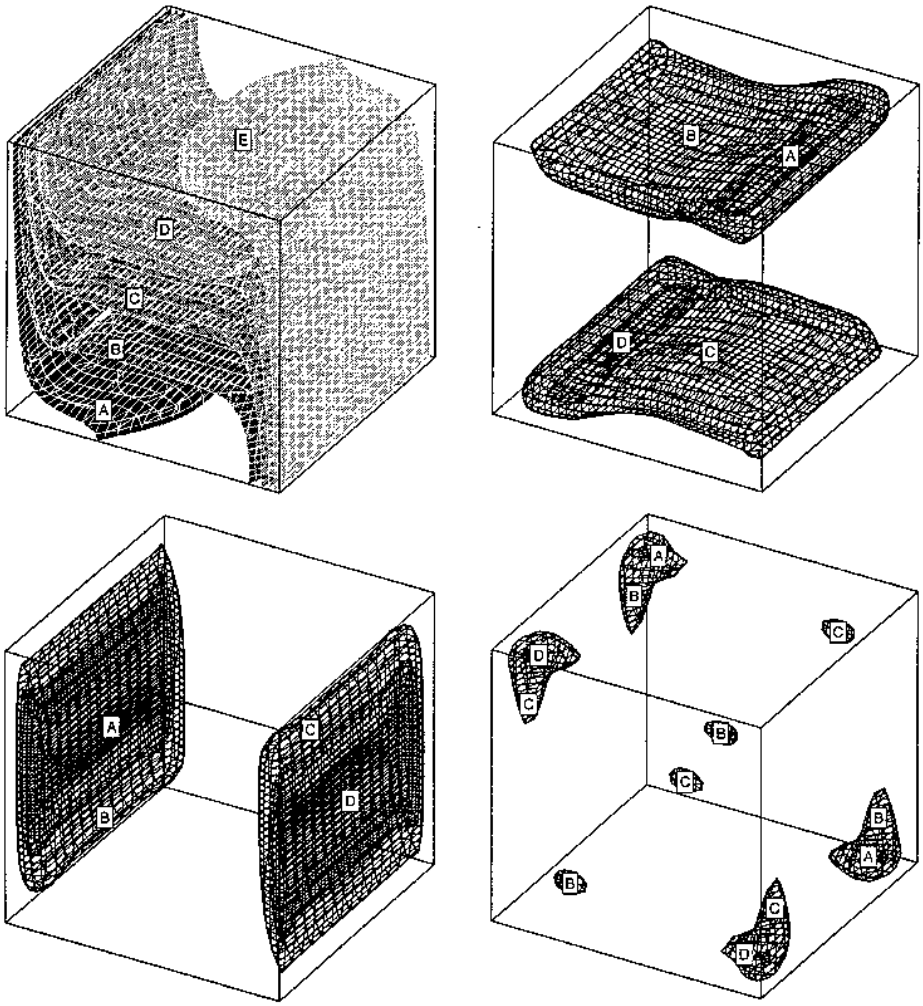

Figure 33. Top left: temperature contours inside the cavity for $Ra = 10^6$. Contour levels: (A) 0.9667, (B) 0.9833, (C) 1.0, (D) 1.017, (E) 1.033. Top right to bottom right: isovelocity contours for *u*-velocity, *v*-velocity and *w*-velocity components respectively for $Ra = 10^6$. Contour levels for *u*: (A) –0.12, (B) –0.06, (C) 0.06, (D) 0.12. Contour levels for *v*: (A) –0.2, (B) –0.1, (C) 0.1, (D) 0.2. Contour levels for *w*: (A) –0.024, (B) –0.012, (C) 0.012, (D) 0.024

4. Chorin, A.J., "A numerical method for solving viscous incompressible flow problems", *Journal of Computational Physics*, Vol. 2, 1967, pp. 12-26.
5. Hoffmann, K.A., *Computational Fluid Dynamics for Engineers*, Engineering Education System, Austin, TX, 1989.
6. Shaw, H., "Laminar mixed convection heat transfer in three-dimensional horizontal channel with a heat bottom", *Numerical Heat Transfer, Part A*, Vol. 23, 1993, pp. 445-61.
7. Ramaswamy, B., Jue, T.C. and Akin, J.E., "Finite element analysis of oscillatory flow with heat transfer inside a square cavity", *AIAA Journal*, Vol. 30, 1992, pp. 412-22.
8. Pepper, D.W., "Modelling of three-dimensional natural convection with a time-split finite-element technique", *Numerical Heat Transfer*, Vol. 11, 1987, pp. 31-55.
9. Fusegi, T., Hyun, J.M., Kuwahara, K. and Farouk, B., "A numerical study of 3-D natural convection in a differentially heated cubical enclosure", The Winter Annual Meeting of the American Society of Mechanical Engineers, 25-30 November, *Heat Transfer Division*, Vol. 157, 1990, pp. 49-54.